Published in final edited form as:

Mol Cell. 2021 November 04; 81(21): 4509–4526.e10. doi:10.1016/j.molcel.2021.08.039.

PKCλ/ι inhibition activates an ULK2-mediated interferon response to repress tumorigenesis

Juan F. Linares[1], **Xiao Zhang**[1], **Anxo Martinez-Ordoñez**[1], **Angeles Duran**[1], **Hiroto Kinoshita**[1], **Hiroaki Kasashima**[2], **Naoko Nakanishi**[3], **Yuki Nakanishi**[4], **Ryan Carelli**[1], **Luca Cappelli**[1], **Esperanza Arias**[5], **Masakazu Yashiro**[2], **Masaichi Ohira**[2], **Sanjay Patel**[1], **Giorgio Inghirami**[1], **Massimo Loda**[1], **Ana Maria Cuervo**[5], **Maria T. Diaz-Meco**[1,*], **Jorge Moscat**[1,6,*]

[1]Department of Pathology and Laboratory Medicine and Sandra and Edward Meyer Cancer Center, Weill Cornell Medicine, New York, NY 10065, USA

[2]Department of Gastroenterological Surgery, Osaka City University Graduate School of Medicine, 1-4-3 Asahimachi, Abeno-ku, Osaka city 545-8585, Japan

[3]Department of Endocrinology and Metabolism, Graduate School of Medical Science, Kyoto Prefectural University of Medicine, Kyoto, Japan

[4]Department of Gastroenterology and Hepatology, Kyoto University Graduate School of Medicine, Kyoto, Japan

[5]Departments of Medicine and of Developmental and Molecular Biology and Institute for Aging Studies, Albert Einstein College of Medicine, Bronx, NY 10461, USA

[6]Lead Contact

SUMMARY

The interferon (IFN) pathway is critical for cytotoxic T cell activation, which is central to tumor immunosurveillance and successful immunotherapy. We demonstrate here that PKCλ/ι inactivation results in the hyper-stimulation of the IFN cascade and the enhanced recruitment of CD8+ T cells that impaired the growth of intestinal tumors. PKCλ/ι directly phosphorylates and represses the activity of ULK2, promoting its degradation through an endosomal microautophagy-driven ubiquitin-dependent mechanism. Loss of PKCλ/ι results in increased levels of enzymatically active ULK2 that by direct phosphorylation activates TBK1 to foster the activation of the STING-mediated IFN response. PKCλ/ι inactivation also triggers autophagy that prevents STING degradation by chaperone-mediated autophagy. Thus, PKCλ/ι is a hub regulating

*Correspondence: jom4010@med.cornell.edu (J.M.); mtd4001@med.cornell.edu (M.T.D.-M.).

AUTHOR CONTRIBUTIONS

Conceptualization, J.M., M.T.D.-M., and J.F.L.; Methodology, J.M., M.T.D.-M., and J.F.L.; Investigation, J.F.L., X.Z., A.M-O., A.D., H. Kinoshita., H. Kasashima., N.K., Y.N., S.P., R.C., and E.A.; Resources, M.Y., and M.O.; Writing-Original Draft, J.M., M.T.D.-M., and J.F.L.; Writing-Review & Editing, all authors; Supervision, J.M., M.T.D.-M., M.L., A.M.C., L.C., and G.I.; Funding Acquisition, J.M. and M.T.D.-M.

DECLARATION OF INTERESTS

The authors declare no competing interests.

the IFN pathway and three autophagic mechanisms that serve to maintain its homeostatic control. Importantly, single cell multiplex imaging and bioinformatics analysis demonstrated that low PKCλ/ι levels correlate with enhanced IFN signaling and good prognosis in colorectal cancer patients.

In Brief

Linares et al. describe how PKCλ/ι loss activates intestinal epithelial ULK2 and leads to its accumulation by inhibiting its degradation by microautophagy. Activated ULK2 phosphorylates TBK1 to promote the STING-mediated IFN signaling that triggers a $CD8^+$ anti-tumor response. Activation of macroautophagy by PKCλ/ι deficiency prevents STING degradation by chaperone-mediated autophagy.

Graphical Abstract

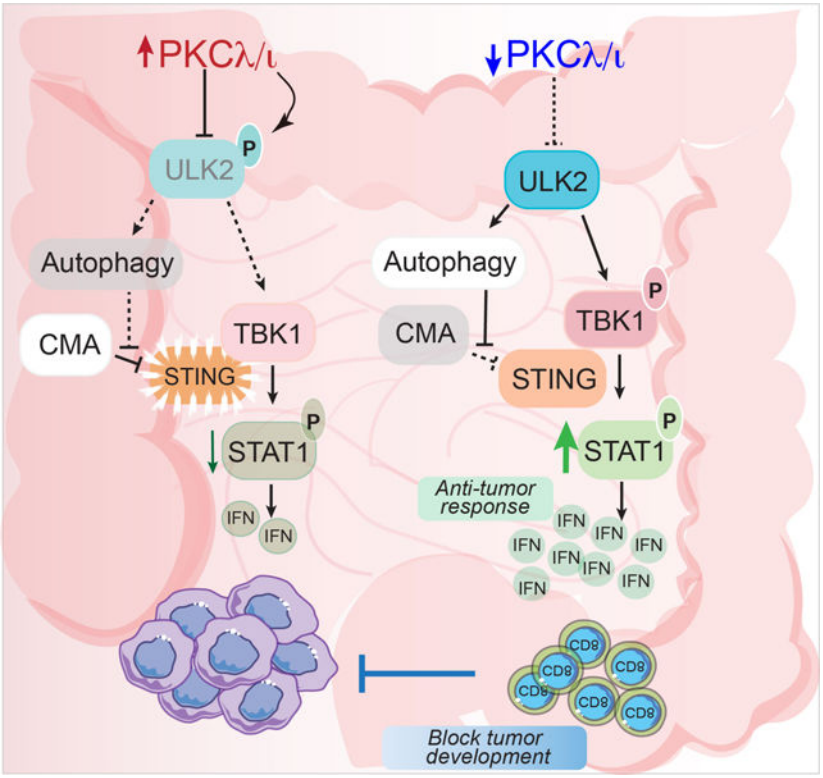

INTRODUCTION

Immunosurveillance is one of the critical mechanisms that restrict tumor initiation but, as cancer progresses, it is impaired and often substituted by an immunosuppressive microenvironment (Dersh et al., 2021; Vitale et al., 2021). In colorectal cancer (CRC), as in many other types of neoplasia, the presence of tumor-infiltrating lymphocytes indicates a favorable prognosis (Gentles et al., 2015; Mlecnik et al., 2016). CRC is a paradigmatic example of the role of different types of immune responses in the genesis and development of the disease and their potential therapy (Bruni et al., 2020). Despite improvements in

systemic treatment, CRC is a major cause of cancer mortality worldwide with a 5-year survival rate of only 12%–14% for those diagnosed with distant-stage disease (Martini et al., 2020). The general consensus is that genome instability and hypermutation-generated neoantigens theoretically predict a favorable response to immunotherapy (Germano et al., 2017; Le et al., 2017; Mandal et al., 2019). Unfortunately, many patients harboring high tumor mutational burden cancers do not respond to this type of therapeutic strategies (Martini et al., 2020).

Although immunotherapy has been approved for MSI-H patients, 60% of these individuals fail to respond to immune checkpoint blockade (ICB) (Bruni et al., 2020; Overman et al., 2017). The fact that MSI-H CRC only comprise 14% of all CRC, together with the evidence that the vast majority of CRC cases fall in the MSS category, which are refractory to immunotherapy, makes ICB effective only in a very small proportion of patients (Bruni et al., 2020; Le et al., 2017; Overman et al., 2017). An emerging notion in the CRC field is that a mesenchymal phenotype of the tumor epithelium, together with an immunosuppressive and desmoplastic stroma, predicts adverse outcomes in CRC patients better than the presence of prevalent mutations (Jones et al., 2008; Mlecnik et al., 2016; Siegel et al., 2017). Thus, key features of the tumor microenvironment (TME), such as the lack of T cell infiltration, increased immunosuppression, and a highly mesenchymal phenotype with desmoplastic stroma, predict adverse outcomes in CRC patients (Calon et al., 2015; Galon et al., 2006; Tosolini et al., 2011). Indeed, these are defining characteristics of the poor prognosis CMS4 subtypes, according to the most recent transcriptomic classifications of different CRCs (De Sousa et al., 2013; Guinney et al., 2015). Furthermore, CMS2 and CMS3 CRCs are “cold” from an immunological point of view, while tumors in CMS4 mouse models can only be reduced by anti-PD-L1 treatment if the immunosuppressive microenvironment is simultaneously inhibited with anti-TGFβ cotreatment or by blocking suppressor myeloid cells (Liao et al., 2019; Nakanishi et al., 2018; Tauriello et al., 2018). These observations suggest that immunotherapy might be an effective way to treat CRC aggressive tumors if immunosurveillance mechanisms are upregulated. Therefore, although immunotherapy holds the promise of a cure or at least better treatments for CRC and other cancers, still much needs to be understood about how to boost the anti-tumor immune response and to prevent immunosuppression.

We have recently reported that when the atypical protein kinase C (aPKC) λ/ι isoform (PKCλ/ι) is selectively deleted in intestinal epithelial cells (IECs; *Prkci-Villin-Cre*), mice develop intestinal inflammation and an infiltration of $CD8^+$ T cells (Nakanishi et al., 2018). While these mutant mice do not develop tumors, depletion of $CD8^+$ T cells results in the generation of spontaneous intestinal carcinomas with serrated CMS4 characteristics (Nakanishi et al., 2018). These results indicate that while the loss of PKCλ/ι in IECs activates inflammation-driven pro-tumor signals, it simultaneously triggers $CD8^+$ T-cell mediated immunosurveillance mechanisms that prevent tumor initiation (Nakanishi et al., 2018). The study of the *Prkci-Villin-Cre* mice revealed that although PKCλ/ι deficiency is protumorigenic under conditions of immunosuppression, its ability to promote the recruitment of $CD8^+$ T cells is a potent deterrent for tumor development (Nakanishi et al., 2018). What remains to be tested is whether inhibiting PKCλ/ι will trigger a cancer inhibitory immune response sufficient to shrink already established tumors, which would

be consistent with PKCλ/ι being a therapeutic target in cancer by boosting anti-neoplastic immune responses in CRC. Therefore, unraveling the mechanisms of action of this PKC isoform will generate critical information on how to enhance cytotoxic T cells to restrain tumorigenesis either alone or in combination with other therapies. Here we have addressed this fundamental question and determined the mechanisms whereby PKCλ/ι controls immunosurveillance that blunt tumor initiation and progression.

RESULTS

PKCλ/ι deficiency results in the upregulation of the IFN pathway in intestinal epithelial cells

Gene set enrichment analysis (GSEA) and NextBio interrogation of the transcriptome of IECs from mice with the selective deletion of PKCλ/ι in the intestinal epithelium (*Prkci*$^{f/f}$; *Villin-Cre*), revealed the upregulation of signatures indicative of IFN pathway activation (Figures 1A and S1A-1C). Chromatin accessibility analysis (ATAC-seq) combined with the RNA-seq data using the PageRank algorithm Taiji (Zhang et al., 2019) identified IFN-related TFs as key drivers of the enhanced IFN response phenotype in *Prkci*$^{f/f}$; *Villin-Cre* IECs (Figure 1B). To investigate the cell autonomous effect of PKCλ/ι loss in the activation of the IFN cascade, we generated organoids from inducible *Prkci*$^{f/f}$; *Villin-Cre*ER mice, which showed increased expression of IFN-stimulated genes (ISGs) upon tamoxifen treatment (Figures 1C and 1D). GSEA of transcriptomics data of tumor organoids (MTOs) with simultaneous mutations in *Apc*, *Trp53*, *Kras*, and *Tgfbr2* (Tauriello et al., 2018), and deletion of *Prkci* by CRISPR/Cas9 showed enrichment of IFN signatures (Figures S1D-S1F). PCR analysis confirmed the upregulation of ISGs in PKCλ/ι-deficient MTOs (Figures S1G). Therefore, the loss of PKCλ/ι in the intestinal epithelium results in the cell-autonomous upregulation of IFN signaling.

PKCλ/ι-deficiency in the intestinal epithelium drives IFN activation and anti-cancer immunosurveillance in vivo

Immunohistochemical (IHC) analysis of *Prkci*$^{f/f}$; *Villin-Cre* intestines showed strong IFN activation, as determined by pSTAT1 (Figure 1E). Tamoxifen treatment of *Prkci*$^{f/f}$; *Villin-Cre*ER mice also resulted in increased pSTAT1 in the IEC compartment (Figures 1F and 1G). The IFN pathway is instrumental for the induced recruitment and stimulation of $CD8^+$ T cells (Dersh et al., 2021; Vitale et al., 2021). Consistently, tamoxifen-treated *Prkci*$^{f/f}$; *Villin-Cre*ER mice displayed abundant intestinal infiltration of $CD8^+$ T cells as compared to controls (Figure 1H). Enhanced recruitment of $CD8^+$ T cells was also observed in the lamina propria (Fig. S1H). Increased IFN and $CD8^+$ infiltration is associated with enhanced anti-tumor immunosurveillance (Dersh et al., 2021; Vitale et al., 2021). Therefore, we posited that the inducible genetic inactivation of PKCλ/ι in IECs will negatively impact the growth of established intestinal tumors. To test this hypothesis, we subjected *Prkci*$^{f/f}$; *Villin-Cre*ER mice to the azoxymethane (AOM)/dextran sulfate sodium salt (DSS) protocol (Kasashima et al., 2020). At the completion of the AOM/DSS treatment, when tumors were visible by colonoscopy, mice were intraperitoneally injected with tamoxifen and sacrificed four weeks thereafter (Figure 1I). IHC of PKCλ/ι showed the efficient deletion of *Prkci* upon tamoxifen injection (Figure S1I). The inducible deletion of PKCλ/ι

in IECs resulted in reduced tumor burden (Figures 1J and 1K), which correlated with increased pSTAT1 and recruitment of $CD8^+$ T cells (Figures 1L and 1M). Next, mice were subcutaneously transplanted with syngeneic MC38 cells with *Prkci* deleted by CRISPR/Cas9 (Figure 1N). *sgPrkci* MC38 cells showed reduced tumor volume concomitant with increased pSTAT1 and infiltration of CD8+ T cells (Figures 1O–1Q). Similar results were obtained with subcutaneous transplantation of MTO sgC and sg*Prkci* (Figures 1R–1U). These results demonstrate that the increased IFN response triggered by the inactivation of PKCλ/ι in the intestinal epithelium results in reduced tumorigenesis associated with increased infiltration of $CD8^+$ T cells.

PKCλ/ι interaction with ULK2 is critical for the control of the IFN response through TBK1

cGAS is the cellular sensor of dsDNA that produces the second messenger cGAMP to activate STING in the endoplasmic reticulum (ER) (Ishikawa and Barber, 2008; Sun et al., 2013). Upon activation, STING translocates to the Golgi where polymerizes to recruit and activate TBK1, which phosphorylates itself, STING and, subsequently, the interferon regulatory factor 3 (IRF3) (Hopfner and Hornung, 2020). Phosphorylated IRF3 controls the transcriptional activation of type I IFNs that triggers the phosphorylation and activation of STAT1 (Burdette and Vance, 2013; Hopfner and Hornung, 2020) (Figure 2A). The whole signaling cascade, including increased levels of STING and its phosphorylated form, was upregulated in dsDNA-treated sg*Prkci* MC-38 cells as compared to control cells (Figure 2B). Similar results were obtained in the mouse non-tumor immortalized MODE-K cell line (Figure 2C), which resulted in increased ISGs expression in response to dsDNA (Figure S2A). Augmented levels of IFN transcripts were also detected in sg*Prkci* MC38 (Figure S2B) and in IECs from *Prkci*$^{f/f}$;*Villin-Cre* mice (Figure S2C). Increased IFN signaling was observed in HEK293 cells that are responsive to cGAMP (Zhang et al., 2014), which indicates that PKCλ/ι impacts the IFN cascade upstream of TBK1 but downstream of cGAS (Figures 2A and 2D). Accumulation of STING was observed in vivo upon deletion of PKCλ/ι in IHC of intestines of *Prkci*$^{f/f}$;*Villin-Cre* and *Prkci*$^{f/f}$;*Villin-Cre*ER mice (Figures 2E and 2F).

To dissect the mechanism, we carried out an unbiased approach to identify partners of PKCλ/ι using the proximity-dependent biotin method (BioID2). p62/SQSTM1, a well-known partner of PKCλ/ι (Moscat et al., 2016; Sanchez et al., 1998), was identified among the most significant interactors in this screening, validating this approach (Figure 2G). Pathway enrichment analysis using the REACTOME database (https://reactome.org/) identified autophagy, in keeping with our recently published data (Kudo et al., 2020; Moscat and Diaz-Meco, 2020), and intracellular trafficking from the endoplasmic reticulum to the Golgi (Figures 2G, S2D and S2E). This screening also identified ULK2 (Fig. 2G), which together with ULK1, is not only involved in autophagy but also in IFN signaling (Lee and Tournier, 2011; Saleiro et al., 2015). We confirmed that ULK2 binds PKCλ/ι by immunoprecipitation of ectopically expressed proteins (Figure 2H). Knockdown of *Ulk2*, but not of *Ulk1*, rescued the enhanced dsDNA-induced IFN signaling by PKCλ/ι deficiency, including STING phosphorylation (Figures 2I and S2F), as well as ISGs expression in MODE-K and MC38 cells (Figures S2G and S2H). Previous studies suggested that ULK1 can activate TBK1 by phosphorylation of S172 (Zhao et al., 2018). Because the

strong similarity between both ULK isoforms, we tested whether TBK1 could also be a substrate of ULK2. An in vitro kinase assay using recombinant ULK2 confirmed that ULK2 phosphorylates TBK1 at S172 (Figure 2J). Consistently, the ability of ULK2 to phosphorylate TBK1's S172 was more prominent when ULK2 was immunoprecipitated from sg*Prkci* HEK293T cells than from sgC cells (Figure 2K). This increased activation of TBK1 in PKCλ/ι-deficient cells is responsible for the enhanced phosphorylation of STING in these cells (Figure 2I). Knockdown of TBK1 reverted pSTING levels in dsDNA-stimulated sg*Prkci* cells to those of basal controls (Figure 2L). ULK2 was required for the formation of the TBK1-STING complex (Figure 2M), whereas loss of PKCλ/ι increased it (Figure 2N). These data support a model whereby PKCλ/ι deficiency promotes the activation ULK2, which renders TBK1 active by S172 phosphorylation, triggering its association with STING, a critical event in IRF3 phosphorylation and activation.

The pharmacological inhibition of ULK1/2 reduces the IFN response promoted by PKCλ/ι-deficiency

Treatment of dsDNA-stimulated cells with a ULK1/2 pharmacological inhibitor (SBI-0202965; (Egan et al., 2015)) impaired the phosphorylation of TBK1, IRF3, STAT1 and STING (Figure 3A). Although SBI-0202965 is a 5–10 fold more potent inhibitor of ULK1 than ULK2 (Egan et al., 2015), given that the knockdown of *Ulk2* but not *Ulk1* reversed the effect of sg*Prkci* in MODE-K cells (Figure 2I), our results provide pharmacologic validation of the role of ULK2 in the activation of the IFN response and suggest that SBI-0202965 effectively targets ULK2 activation in this system. To analyze the effect of the ULK1/2 inhibitor in vivo, we treated *Prkci*$^{f/f}$; *Villin-Cre* and *Prkci*$^{f/f}$ mice with SBI-0202965, which reduced the enhanced IFN response in these mutant mice, as determined by pSTAT1 and STING IHC (Figures 3B–3D). Western blot analysis of pTBK1, pSTAT1 and STING or qPCR of ISGs mRNA of isolated IECs showed complete impairment of the IFN-induced signaling in ULK inhibitor-treated samples (Figures 3E and 3F). Furthermore, the in vivo treatment also abolished the enhanced infiltration of CD8^{+} T cells in *Prkci*$^{f/f}$; *Villin-Cre* intestinal tissues to levels comparable to those of WT mice (Figure 3G). These data demonstrate the biological relevance of the PKCλ/ι-ULK2-TBK1 axis in the control of the IFN response.

PKCλ/ι directly represses ULK2 kinase activity

Re-expression of WT PKCλ/ι but not a PKCλ/ι kinase-inactive mutant repressed the upregulation of the IFN signaling cascade in sg*Prkci* cells, demonstrating that the kinase activity of PKCλ/ι is necessary for its role in the IFN pathway. In keeping with this, an in vitro kinase assay using ULK2 with active PKCλ/ι demonstrated that ULK2 is a direct substrate of PKCλ/ι (Figure 4B). Interrogation of the ULK2 sequence using Scansite v4.0 (https://www.scansite4.mit.edu) identified eight potential aPKC consensus motifs (Figure 4C). S150 was previously reported in the mass spectrometry database PhosphoSitePlus (https://www.phosphosite.org), it is conserved across species, and is part of the aPKC consensus phosphorylation sequence (Figure 4D). Mutation of S150 to alanine significantly reduced ULK2 phosphorylation by PKCλ/ι, indicating that ULK2's S150 is indeed a bona fide site for PKCλ/ι (Figure 4E). MutPred2 (http://mutpred.mutdb.org/) analysis predicted that S150D mutation would result in the loss of the catalytic site at K155 (Figure 4F).

Indeed, ULK2-S150A phosphorylated more efficiently TBK1 than ULK2-WT, while ULK2-S150D activity was even lower than that of WT ULK2 (Figure 4G). CRISPR/Cas9-mediated editing of endogenous ULK2's S150 to alanine in MODE-K cells (ULK2^{S150A} cells; Figure 4H) resulted in increased phosphorylation of TBK1, IRF3, and STAT1, and enhanced ISGs expression (Figures 4I–4K). These data indicate that PKCλ/ι represses IFN signaling through the negative regulation of the ULK2 kinase activity by direct phosphorylation of its S150.

PKCλ/ι regulates ULK2 levels through a ubiquitin-dependent lysosomal degradation mechanism

PKCλ/ι deficiency also resulted in higher amounts of ULK2 protein, but not mRNA levels (Figures 5A, 5B and S3A-S3D), which indicated that PKCλ/ι might regulate ULK2 stability. Consistently, the expression of ULK2 with different amounts of PKCλ/ι resulted in ULK2 degradation in a dose-dependent manner (Figure 5C). ULK2-S150A was also significantly more stable in cycloheximide-treated cells than WT ULK2 (Figures 5D and 5E). Treatment with the lysosomal inhibitor Bafilomycin A1, but not with the proteasome inhibitor MG132 or the ER-Golgi trafficking inhibitor Brefeldin (BFA), resulted in increased ULK2 levels, suggesting a lysosome-dependent mechanism (Figures 5F and 5G). Knocking down critical regulators of macroautophagy, endosomal-microautophagy, and chaperone-mediated autophagy (CMA), using specific siRNAs for *Atg5*, *Vps4AB*, and *Lamp2-a*, respectively, demonstrated that the knockdown of *Vps4AB* has the same effect as Bafilomycin A1 treatment on ULK2 protein levels (Figures 5F and 5G), suggesting that ULK2 is degraded primarily through endosomal-microautophagy. The accumulation of ULK2 in si*Vps4AB* cells is comparable to that in PKCλ/ι-deficient cells (Figures 5H and 5I). While inhibition of the proteasome has not detectable effect on ULK2 levels (Figures 5F and 5G), however, ubiquitination could direct proteins for lysosomal degradation (Ciechanover, 2015). In fact, ULK2 ubiquitination was impaired in sg*Prkci* and in ULK2^{S150A} cells (Figures 5J and 5K). Expression of a K63R ubiquitin mutant (that is unable to create K63-linked ubiquitin chains) impaired ULK2 ubiquitination, whereas a K48R mutant (unable to create K48-linked chains) did not (Figure 5L), which demonstrated that ULK2 ubiquitination takes place through K63 conjugation.

To elucidate the mechanism whereby PKCλ/ι regulates ULK2 ubiquitination, we interrogated BioID interactome (Figures 2G and 5M), which identified NDFIP1 (NEDD4 family interacting protein 1) as a PKCλ/ι interacting partner (Figure 5M). NDFIP1 functions both as an adaptor and an activator of multiple NEDD4 E3 ubiquitin ligases (Putz et al., 2008). Since PKCλ/ι interacts with NDFIP1, PKCλ/ι could bridge the interaction between one of the members of the NEDD4 family and ULK2 to promote its ubiquitination and subsequent lysosomal-mediated degradation. To test this, we first confirmed that NDFIP1 interacts with PKCλ/ι in immunoprecipitation assays with ectopically expressed proteins (Figure 5N). Also, knockdown of *Ndfip1* resulted in increased ULK2 levels, and increased dsDNA-induced IRF3 and STAT1 phosphorylation (Figures 5O and 5P), indicating a critical role for NDFIP1 in ULK2 stability and the IFN pathway. Among the NEDD4 family members, NEDD4 and NEDD4L preferentially ubiquitinate substrates through K63 conjugation (Huang et al., 2019). Therefore, we tested the contribution of

NEDD4L and NEDD4 to ULK2 stability. Knockdown of *Nedd4l,* but not of *Nedd4,* has the same effect as *Ndfip1* knockdown on ULK2 protein levels (Figure 5Q), suggesting that NEDD4L is the ubiquitin ligase involved in the control of ULK2 stability. Consistently, *Nedd4l* downregulation impaired ULK2 ubiquitination (Figure 5R), and NDFIP1 co-immunoprecipitated with PKCλ/ι and ULK2 in microautophagy-deficient cells (Figure 5S). MutPred2 (http://mutpred.mutdb.org/) predicts a gain of ubiquitination at K146 in the ULK2 S150D mutant (Figure 5T), which is consistent with an impairment in the ubiquitination of ULK2 in PKCλ/ι-deficient and ULK2^{S150A} cells (Figures 5J and 5K). K146 is the residue most likely to be ubiquitinated in ULK2, as predicted by the iUbiq-Lys site (http://www.jci-bioinfo.cn/iUbiq-Lys). Mutation of K146 to alanine impaired ULK2 ubiquitination and enhanced its stability (Figures 5U–5W). These data demonstrated that ULK2 phosphorylation by PKCλ/ι at S150 serves to promote its K63 ubiquitination at K146 in an NDFIP1-NEDD4L dependent manner, which is critical for the control of ULK2 levels and activity, and the ensuing activation of the IFN cascade (Figure 5X).

PKCλ/ι represses autophagy through an ULK2-dependent mechanism

Consistently with the BioID2 data linking autophagy and PKCλ/ι (Figure 2G and S2D), sg*Prkci* cells had higher basal levels of LC3-II and increased LC3-II lysosomal degradation, consistent with enhanced autophagic flux, mainly due to higher rates of autophagosome biogenesis (difference in LC3-II levels once lysosomal degradation is already blocked) both under basal (serum+) and inducible (serum-) conditions (Figures 6A–6C). To examine efficient autophagosome (APG) maturation into autolysosomes (AUT), we next used a tandem fluorescent-tagged LC3 reporter (mCherry-GFP-LC3) that allows the identification of APG (vesicles positive for both fluorophores) and AUT (vesicles positive only for mCherry since GFP fluorescence is quenched at the acid pH of the lysosome). sg*Prkci* MODE-K cells displayed higher overall abundance of APG and AUT both under basal conditions and in response to nutrient deprivation, thus confirming their overall increase in autophagic flux through increased APG formation coupled with their efficient clearance by lysosomes (Figure S4A). Immunoblot analysis of crypts from *Prkci*$^{f/f}$;*Villin-Cre* mice demonstrated higher levels of LC3 and of its lipidated form, LC3-II than in *Prkci*$^{f/f}$ mice, which was more apparent upon treatment with Bafilomycin A1 to block lysosomal function or with the mTORC1 inhibitor rapamycin, a bona fide inducer of autophagy (Figures S4B-4D). Electron microscopy and morphometric analyses of sg*Prkci* MODE-K cells confirmed higher abundance of both APG and AUT compared to controls (Figures 6D and 6E). The increase in autophagic compartments was more noticeable under basal conditions (serum supplemented cells), whereas upon serum removal higher rates of autophagy in these cells seem to be attained by recruitment of endocytic compartments, as we observed a significant increase in the amount of amphisomes (AMPH; resulting from the fusion of autophagosomes with late endosomes) and late/endosome multivesicular bodies in sg*Prkci* cells (Figures 6F and 6G). We next tested whether the upregulation of ULK2 by PKCλ/ι deficiency was required for the enhanced autophagic flux in sg*Prkci* cells. *Ulk2* knockdown reverted the increase in the LC3 flux and APG biogenesis in sg*Prkci* cells (Figures 6H–6J). ULK2^{S150A} expression was sufficient to increase autophagy flux through higher autophagosome biogenesis (Figures 6K–6M), mimicking the enhancement

of autophagy found in sg*Prkci* cells (Figures 6A–6C). These data indicate that PKCλ/ι represses autophagy through the negative regulation of S150 ULK2 phosphorylation.

We next determined whether autophagy plays any role in the regulation of the IFN cascade under conditions of PKCλ/ι deficiency. Knockdown of key autophagy regulators such as ATG5, ATG16L1 or p62, significantly reduced dsDNA-induced IFN pathway, particularly under conditions of PKCλ/ι deficiency (Figures 6N and 6O). Inhibiting autophagy rendered cells with reduced levels of STING and blocks its phosphorylation (Figure 6O). Previous studies showed that STING degradation by chaperone-mediated autophagy contributes to the downregulation of the IFN pathway (Hu et al., 2016). To elucidate if upregulation of autophagy upon PKCλ/ι loss contributes to stabilize STING by preventing its degradation by CMA, we analyzed the effect of *siLamp2A* on STING levels in a context of intact or blocked autophagy. We found that the reduction in STING levels upon autophagy blockade was rescued by inhibiting CMA, which restored the IFN cascade in autophagy-deficient MODE-K cells to the levels of sgC cells (Figures 6P and 6Q). These results support the concept that the increased autophagy in PKCλ/ι-deficient cells serves to sustain the activation of the IFN pathway by preventing STING degradation by CMA (Figure 6R). Consistent with this model, PKCλ/ι loss resulted in increased STING stability (Figures S4E and S4F).

PKCλ/ι-IFN connection in human cancer

To establish the relevance of the increased PKCλ/ι-IFN link in human CRC, we analyzed patient RNA-seq data from the TCGA dataset (TCGA-COREAD). We first stratified patients according to the expression of *PRKCI* and performed GSEA. Patients with low *PRKCI* were significantly enriched in multiple signatures of the IFN activation pathway (Figures 7A and 7B). *PRKCI* expression was also found highly correlated with multiple ISGs in human CRC samples (Figure S5A). Bioinformatics interrogation of single-cell RNAseq data of twenty-three CRC patients classified based on the expression of *PRKCI* revealed significant enrichment in the IFN response and allograft rejection signatures in the tumor epithelial cells expressing low levels of *PRKCI* (Figures 7C-7E). We also found a negative correlation between *PRKCI* mRNA levels and an autophagy-lysosome signature in the TCGA-COREAD data set (Figure 7F).

To further support the human relevance of our findings, we performed VECTRA multiplex imaging to interrogate the correlations, at a single cell level, of PKCλ/ι expression with the IFN response and recruitment of CD8 T cells in a CRC tissue microarray (TMA) of 147 patients (Figure S5B). We used DAPI as a nuclear marker, cytokeratin to label epithelial cells, CD8 to identify CD8 T cells, pSTAT1 as a marker for the IFN response, and PKCλ/ι (Figure S5C). Validation of our antibody panel and the imaging pipeline are shown in Figures S5B-S5E. The pipeline analysis included spectral separation of the signal generated in VECTRA, deconvolution and segmentation of cells using DAPI (Figure S5F) and generation of single cell data (Figure S5G). To test whether the loss of PKCλ/ι in the tumor epithelium is associated with more IFN response, we categorized epithelial cells (CK positive cells) based on PKCλ/ι levels in two groups: PKCλ/ι positive and PKCλ/ι negative. Next, we quantified the relative proportions of pSTAT1 positive cells in these two

groups (Figure 7G). Rank-sum Wilcoxon differential expression test found that pSTAT1 was differentially expressed in $CK^+/PKC\lambda/\iota^+$ vs. $CK^+/PKC\lambda/\iota^-$ with log fold change of −0.619 ($p < 0.01$). This suggested that epithelial cells expressing low levels of PKCλ/ι were activating the IFN pathway, as measured by pSTAT1, as compared to high PKCλ/ι expressors. Next, we tested whether this activation of the IFN pathway in PKCλ/ι low cells correlated with an increment of $CD8^+$ T cells recruitment. VECTRA images were analyzed for the spatial coordinates of each cell within the tissue. We visualized the frequency of $CD8^+$ T cells in the vicinity of epithelial cells (Figure 7H), and computed neighborhood enrichments. $CD8^+$ T cells were more enriched in the neighborhood of $PKC\lambda/\iota^{low}$ regions than of $PKC\lambda/\iota^{high}$ regions ($p<0.01$, Wilcoxon signed rank test) (Figure 7I). These data demonstrate in human CRC that the loss of PKCλ/ι in the CRC epithelium activates the IFN response that results in an increased recruitment of $CD8^+$ T cells.

We next investigated whether low amounts of *PRKCI* correlates with clinical outcome in CRC by stratifying patients of the TCGA-COREAD cohort by levels of *PRKCI*. CRC patients with low levels of *PRKCI* had a better prognosis than those with high levels of *PRKCI* (Figure 7J). Given that the loss of *PRKCZ* has been shown to impair the immune surveillance mechanisms activated by the loss of *PRKCI* (Nakanishi et al., 2018), we stratified further this CRC cohort considering the levels of *PRKCZ*. This analysis demonstrated that among patients with high PRKCZ levels, those with low *PRKCI* showed better disease-free survival than those with high *PRKCI* (Figure 7K). Classification of patients based on their expression score of the IFN response predicts better outcome for patients expressing high levels of IFN (Figure 7L).

Intestinal chronic inflammatory diseases are associated with an elevated risk of CRC. Therefore, we investigated the link between PKCλ/ι and the IFN cascade in the context of inflammatory bowel diseases (IBD). We found a negative correlation between *PRKCI* expression and IFN gene expression signatures (Figure S5H). IBD patients that do not respond to anti-TNF treatment showed enrichment in IFN activation signatures (Samie et al., 2018) (Figures S5I and S5J), and a concomitant reduction of *PRKCI* expression as compared to responder patients (Figures S5K and S5L). These results demonstrate that *PRKCI* is downregulated in IBD patients, which correlated with a poor response to standard-of-care therapy. We also found that *PRKCI* expression correlated negatively with the autophagy-lysosome signature in IBD (Figure S5M). These results support the human relevance of our findings establishing that PKCλ/ι's role in the intestinal epithelium is to repress both IFN signaling and autophagy, which is critical in the control of CRC development and intestinal inflammation.

DISCUSSION

Numerous studies support the notion that increased immunosurveillance has the power to blunt cancer initiation and to repress the development and progression of already established tumors. It is well known that cytotoxic T cells are central to a successful anti-tumor immune response, for which IFN signaling is a key event (Barber et al., 2006; Benci et al., 2016; Gao et al., 2016). Defects in the IFN pathway in tumors correlate with resistance to ICB (Gao et al., 2016; Zaretsky et al., 2016), which highlights the significance and potential impact

of therapeutic strategies aimed at augmenting the IFN cascade in cancer cells and the tumor microenvironment. Therefore, understanding the mechanisms of IFN activation is key for the design of new ways to boost anti-cancer immune responses. Here we show evidence that PKCλ/ι, through its ability to regulate the IFN pathway, is a critical event in the activation of cancer immunosurveillance and that it could be a therapeutic target in immunotherapy.

The role of PKCλ/ι in cancer is dual (Reina-Campos et al., 2019a). Initial studies showed that its genetic ablation prevents tumor initiation in mouse models driven by potent oncogenes, which led to propose that PKCλ/ι is an important venue for the pro-tumorigenic signals of particular oncogenes such K-Ras or BCR-ABL in lung cancer and chronic myeloid leukemia mouse models, respectively (Reina-Campos et al., 2019a). In marked contrast, *Prkci* inactivation in prostate-specific PTEN KO mice enhanced the tumorigenic potential of PTEN-deficiency, driving the benign phenotype of PTEN null prostate cancer cell towards aggressive adenocarcinomas with neuroendocrine features (Reina-Campos et al., 2019b). Likewise, the selective genetic inactivation of *Prkci* in hepatocytes enhanced tumorigenesis through a mechanism that involved the activation of oxidative phosphorylation, autophagy and the upregulation of the pro-oncogenic transcription factor NRF2 (Kudo et al., 2020; Moscat and Diaz-Meco, 2020). The effects of PKCλ/ι-deficiency in hepatocytes were both cell-autonomous and cell non-autonomous (Kudo et al., 2020). The cell non-autonomous actions of PKCλ/ι loss are particularly important also in intestinal cancer in which, despite a potent carcinogenic effect of PKCλ/ι deficiency, the simultaneous activation of a powerful immunological cytotoxic response prevents tumor initiation (Nakanishi et al., 2018) and shrinks already established intestinal tumors (this paper). Therefore, the unanticipated role of PKCλ/ι as a negative regulator of the IFN pathway could be exploited therapeutically as an anti-cancer mechanism because the stimulation of a potent IFN-$CD8^+$ response upon PKCλ/ι deficiency overrides cell autonomous protumorigenic signals, ultimately resulting in tumor ablation.

Our previous data showed that PKCλ/ι represses autophagy by direct phosphorylation of LC3's S12 in hepatocytes (Kudo et al., 2020; Moscat and Diaz-Meco, 2020). Here we demonstrate that the phosphorylation of ULK2's S150 also contributes to the inhibition of autophagy by PKCλ/ι. Therefore, PKCλ/ι controls autophagy through LC3 and ULK2. Consequently, the inactivation of PKCλ/ι renders IECs with enhanced autophagy and IFN signaling both controlled apically by ULK2. This regulation of autophagy by PKCλ/ι is important for the adequate homeostatic balance of the IFN pathway to stabilize STING by preventing its degradation by CMA (Mlecnik et al., 2016), boosting IFN activation in a feed forward mechanism. In this way, PKCλ/ι inactivation not only directly triggers an augmented IFN cascade at the level of TBK1, but also stabilizes STING to ensure that cells have the adequate levels of this important signaling adaptor for the activation of the TBK1-driven cascade.

Collectively, these findings establish PKCλ/ι as a central node linking endosomal-microautophagy (required for the degradation of ULK2) and macroautophagy (to control STING levels through modulation of its degradation by CMA). These observations have to be considered in the context of previously published and recent data on the immunological role of autophagy, that seems to be context-specific and, in at least some paradigmatic

examples, even involve cell non-autonomous mechanisms still to be fully clarified but that implicate immunotolerance induced by the liver (Bezu et al., 2015; Poillet-Perez et al., 2020; Zhong et al., 2016). However, considering autophagy at the cancer cell-autonomous level, initial studies suggested that it was required for anti-cancer therapies that involved the activation of immunogenic cell death (Bezu et al., 2015; Zhong et al., 2016). In this scenario, inhibiting autophagy would impair chemotherapy (Galluzzi et al., 2017). However, new data suggest that the effect of reducing autophagy in other types of therapy, like radiation, would be the opposite (Yamazaki et al., 2020). Under these conditions, autophagy prevents the accumulation of mitochondrial DNA triggered in response to radiation, which serves to activate the IFN pathway through the cGAS-STING cascade (Yamazaki et al., 2020). In this setting, inhibiting autophagy would boost the IFN response by promoting the accumulation of mitochondrial DNA, which would make radiotherapy more efficient by increasing the immunogenicity of the treated tumor (Yamazaki et al., 2020). Also, autophagy has recently been shown to induce the degradation of MHC-I proteins, at least in pancreatic cancer (Yamamoto et al., 2020), suggesting that inhibiting autophagy prevents immunoevasion and could be a good therapeutic strategy to increase the efficacy of immunotherapy. In the case of PKCλ/ι inhibition, it could be argued that because autophagy is activated, that would promote immunoevasion by decreasing MHC-I protein levels. However, the fact that tumor initiation and progression are blunted by the PKCλ/ι blockade, suggests that the activation of IFN and the induced infiltration of $CD8^+$ T cells is what determines the final outcome of the process in which, in this paradigm, autophagy hyperactivation boosts immunosurveillance. All these observations are of great significance in human disease, since there is a clear negative correlation between PKCλ/ι levels and several signatures of IFN activation and autophagy in patient samples.

Limitations of the Study

Our study establishes a paradigm whereby the loss of PKCλ/ι in the intestinal epithelium upregulates the IFN cascade to promote an anti-tumorigenic response orchestrated by the recruitment of $CD8^+$ T cells. Bioinformatics interrogation of human datasets, and the analysis of TMAs of CRC patients using multiplex immunofluorescence imaging at a single-cell level demonstrate the human relevance of these findings. The mechanism shown here demonstrate the activation and upregulation of ULK2, but not of ULK1, by PKCλ/ι deficiency in several cell systems. In vitro treatment with the ULK1/2 inhibitor SBI-0202965 rescues the enhanced activation of the IFN cascade in PKCλ/ι-deficient cells, although it does not fully abolish it, suggesting that either the conditions used with this inhibitor do not totally block ULK2 activity or there could be other ULK2-independent mechanisms contributing to the observed IFN phenotype upon PKCλ/ι loss. Our in vivo studies using this selective ULK1/2 inhibitor demonstrate that the pharmacological inhibition of ULK activity in vivo blocks the activation of the immunosurveillance mechanisms triggered by PKCλ/ι deficiency in the intestinal epithelium. Although all our in vitro and cell-based studies clearly demonstrate the selective role of PKCλ/ι on the regulation of ULK2 but not ULK1, the fact that the inhibitor used in this in vivo experiment does not distinguishes between both ULK isoforms would require in future studies experiments using mice genetically modified to ablate selectively either ULK genes.

STAR★METHODS

RESOURCE AVAILABILITY

Lead Contact—Further information and requests for resources and reagents should be directed to and will be fulfilled by the Lead Contact, Jorge Moscat (jom4010@med.cornell.edu).

Materials Availability—Cell and mouse lines generated in this study are available from the Lead Contact upon request with a completed Materials Transfer Agreement.

Data and code Availability

- 3' RNA-seq and ATAC-seq data have been deposited at GEO and are publicly available as of the date of publication. Accession numbers are listed in the key resources table. Original raw data have been deposited at Mendeley and are publicly available as of the date of publication. The DOI is listed in the key resources table. This paper analyzes existing, publicly available data. These accession numbers for the datasets are listed in the key resources table.
- This paper does not report original code.
- Any additional information required to reanalyze the data reported in this paper is available from the lead contact upon request.

EXPERIMENTAL MODEL AND SUBJECT DETAILS

Mice—Animal handling and experimental procedures conformed to institutional guidelines and were approved by the Sanford-Burnham-Prebys Medical Discovery Institute Institutional Animal Care and Use Committee, and by the Weill Cornell Medicine Institutional Animal Care and Use Committee. *Prkci*$^{f/f}$ (Leitges et al., 2001; Nakanishi et al., 2016), *Villin-Cre* (Madison et al., 2002), and *Villin-Cre*ERT2 (el Marjou et al., 2004) mice were previously described. *Prkci*$^{f/f}$;*Villin-Cre* and *Prkci*$^{f/f}$;*Villin-Cre*ERT2 mice were generated by breeding *Prkci*$^{f/f}$ mice with *Villin-Cre* mice (Jackson Laboratory, stock number 012641) or *Villin-Cre*ERT2 (Jackson Laboratory, stock number 020282) mice respectively. All mouse strains were generated in a C57BL/6 background and were born and maintained under pathogen-free conditions. All mice were maintained on food and water ad libitum and were age-matched and co-housed for all experiments. Mice were sacrificed and small intestine, colon or other organs were collected for analysis. All genotyping was done by PCR. Age- and sex-matched mice were used for all experiments.

Human Samples—For CRC samples, a total of 147 CRC patients (male, n = 77, average age at diagnosis = 64, age range 29–85; female, n = 70, average age at diagnosis = 66, age range 26–90) who had undergone a resection of the primary tumor at Osaka City University Hospital were analyzed. CRC tissues were obtained from each patient and none of the patients had undergone preoperative radiation or chemotherapy. This study was approved by the Osaka City University Ethics Committee and written informed consent was obtained from patients. De-identified human samples were sent to Weill Cornell Medicine and used

for histological analyses. The study was approved by the IRB Committee of Weill Cornell Medicine.

Cell Lines—HEK293T and Phoenix-GP (sex: female) cell lines were purchased from ATCC. MC38 cell line (sex: female) was purchased from Kerafast. MODE-K cell line (sex: female) was kindly provided by Prof. Blumberg (Harvard Medical School, Boston, USA). Mouse tumor organoids (MTOs) were obtained from Dr. Eduard Batlle (Institute for Research in Biomedicine, Barcelona, Spain) and previously described (Tauriello et al., 2018). HEK293T, Phoenix GP, MODE-K and MC38 cells were cultured in Dulbecco's Modified Eagles Medium (DMEM, Corning) supplemented with 10% fetal bovine serum (FBS), 2 mM glutamine in an atmosphere of 95% air and 5% CO_2. MTOs were cultured in advanced DMEM/F12 medium supplemented with 10 mM HEPES, Glutamax, B-27 (all Life Technologies), 50 ng/ml recombinant human EGF (Peprotech). Normal intestinal organoids were cultured in Advanced DMEM/F12 containing 10 mM HEPES, 1X Glutamax, 1X N2 supplement, 1X B27 supplement, 50 ng/ml EGF, 1000 ng/ml R-spondin 1, 100 ng/ml Noggin, and 10 μM Y-2763 in an atmosphere of 95% air and 5% CO_2. Cultures were tested monthly for mycoplasma contamination.

METHOD DETAILS

Tamoxifen deletion—For induction of *Villin-Cre*ERT2-mediated recombination, mice received one dose of 6 mg of tamoxifen in corn oil by oral gavage and were analyzed 1 week later.

Colitis-Associated Tumorigenesis—For AOM/DSS-induced inflammatory tumorigenesis, 8–10 weeks-old male mice received one intraperitoneal injection of 10 mg/kg AOM (Sigma-Aldrich, St. Louis, MO, USA) in sterile PBS. After 5 days, 2.5% DSS will be given in the drinking water for 5 days, followed by 14 days of regular drinking water. The DSS treatment will be repeated for two additional cycles. Seven days after the third DSS treatment, we perform intraperitoneal injection of 80 mg/kg of tamoxifen 8, 10, 14, 17, 20, 24 and 27 days after the third DSS treatment. Tumor progression after tamoxifen treatment was monitored with colonoscopy and mice were sacrificed four weeks after AOM/DSS treatment. Tumor load was calculated by multiplying tumor number and tumor diameter and were analyzed histologically. All mice were maintained on food and water ad libitum and were age-matched and co-housed for all experiments.

Xenograft Experiments—For mouse xenografts, sg*Prkci* and sgC MC38 cells were trypsinized, washed two times in cold PBS, resuspended in DMEM, aliquoted to 3×10^6 cells per dose in a 150 μl volume and injected subcutaneously into both flanks of WT mice. Tumors were allowed to grow for three weeks. Mice were euthanized three weeks after injection and tumors were analyzed histologically. For xenografts using mouse tumor organoids (MTOs), a 150 μl cell suspension of equivalent to 1×10^6 cells of sg*Prkci* or sgC MTOs admixed with 30% Matrigel (Corning) was directly injected subcutaneously into both flanks of WT mice. Mice were euthanized five weeks after injection and tumors were analyzed histologically.

Flow cytometry analysis—Flow cytometry experiments were performed using fresh small intestinal tissue from 16 weeks-old Villin-CreERT2 1 week after tamoxifen treatment. Briefly, small intestines were rinsed in cold PBS, minced into small pieces, incubated in HBSS with EDTA (30 mM) and HEPES (10 mM), and digested with collagenase (25 mg/ml) and dispase II (25 mg/ml) for 30 min at 37°C, followed by a discontinuous Percoll separation method (40 and 80%) to purify immune cells. The cells concentrated at the interface were collected and washed in cold PBS. Live cells were counted using Trypan blue and then saturated with mouse Fc Block (purified anti-mouse CD16/CD32; 1:50; clone 2.4G2; BD PharMingen) 30 min at 4°C before incubating with specific dyed antibodies: CD45 as a marker for immune cells, βTCR as a T cell maker, NK1.1 to lable NK cells, CD8 and CD4 markers. Flow cytometry experiments were performed on a BD Symphony 29-colors analyzer at the Weill Cornell Medicine Shared Flow Cytometry Core Facility and data were analyzed using FlowJo software (Tree Star Inc.).

Pharmacological Inhibition of ULK1/2 *in vivo*—To analyze the effect of the ULK1/2 (SBI-0202965) inhibitor in vivo, *Prkci*$^{f/f}$ and *Prkci*$^{f/f}$;*Villin-Cre* mice were injected intraperitoneally with 25 mg/kg (mouse bodyweight) of SBI-0202965 or saline twice a week for four weeks before sacrifice. Mice were euthanized and tumors were analyzed histologically.

Cell Culture Experiments—sg*Prcki* HEK293T, MC38 and MODE-K cells were described previously (Nakanishi et al., 2018; Nakanishi et al., 2016). To knock out *Prkci* in mouse tumor organoids (MTOs), single-guide RNA sequences targeting *Prkci* exon1 were purchased from Synthego and transduced into MTOs with recombinant Streptococcus pyogenes Cas9 protein (Truecut Cas9 Protein v2, Thermo), using the Neon Transfection System 1 (Invitrogen) following the manufacturer's protocol and single clones were expanded and screened by protein immunoblotting. To perform *Ulk2* editing in MODE-K cells, single-guide RNA sequences targeting the mouse *Ulk2* gene (Synthego) was transduced into cells with a Cas9 protein and a single-stranded donor oligonucleotide (ssODN, IDT) using Neon Electroporation System. Single clones were expanded and screened for *Ulk2* editing by Sanger sequencing. Knockdown of *p62, tbk1, Atg5, Atg16l1, Vps4, Lamp2-a, Nedd4l, Nedd4, Ndfip1, Ulk1 and Ulk2* genes in MODE-K cells were achieved by siRNA transfection using Lipofectamine RNAiMAX Transfection Reagent (Invitrogen). Transient overexpression was achieved by transfection using X-tremeGENE HP transfection reagent (Roche). Transfected cells were examined 48 h after transfection. Establishing stably FLAG-tagged PKCλ/ι (WT or K274W mutant) expressing MODE-K cells and BioID2-tagged PKCλ/ι (Kudo et al., 2020) expressing HEK293T cells was achieved by retrovirus-mediated transduction. Retroviruses were prepared and used as previously described (Linares et al., 2015). Briefly, retroviruses were produced in Phoenix-GP cells using X-tremeGENE HP transfection reagent (Roche). Virus-containing supernatants were collected 48, 72 and 96 h after transfection, filtered to eliminate cells, and supplemented with 8 μg/ml polybrene. Cells were infected with three rounds of viral supernatants and selected with puromycin (3 μg/ml). For dsDNA and cGAMP stimulation, MODE-K, MC38 or HEK293 cells were transfected with 0.5 μg/ml of dsDNA (IDT) or 10 μg/ml of 2'3'-cGAMP (InvivoGen) or mock using Lipofectamine 2000 (Invitrogen) for the

indicated time. For autophagy inhibition, MODE-K cells were treated for 12 h with 100 nM bafilomycin A1 or vehicle (DMSO). For proteasome inhibition, MODE-K cells were treated for 12 h with 20 μM with MG132 or vehicle (DMSO). For inhibition of the protein trafficking between endoplasmic reticulum (ER) and the Golgi, cells were treated for 12h with 10 μM of Brefeldin or vehicle (DMSO). For the deletion of *Prkci* in normal organoids, 500 nM 4-OH-tamoxifen was added the second day after organoids were passaged.

Histological Analysis—Tissues from indicated mice were isolated, rinsed in ice-cold PBS, fixed in 10% neutral buffered formalin overnight at 4°C, dehydrated, and embedded in paraffin. Sections (5 μm) were stained with hematoxylin and eosin (H&E). For immunohistochemistry, sections were deparaffinized, rehydrated, and then treated for antigen retrieval. After blocking in Protein Block Serum-Free solutions (DAKO), tissues were incubated with primary antibody overnight at 4°C followed by incubation with biotinylated secondary antibody. Endogenous peroxidase was quenched in 3% H202 in water for 10 min at room temperature. Antibodies were visualized with avidin-biotin complex (Vectastain Elite; Vector Laboratories) using diaminobenzidine as the chromogen. Stained sections were analyzed with a Zeiss light microscope supplemented with Axiovision40 software.

BioID2-Based Screening—HEK293T cells stably expressing myc-BioID2 or myc-BioID2-PKCλ/ι were incubated for 8 h in the presence of 50 μM biotin and stimulated with 0.5 μg/ml of dsDNA (IDT) or mock for the last 6 h. Cells were then washed three times with PBS, pelleted and kept at −20°C. Cell pellets were lysed via sonication in 8M urea, 50 mM ammonium bicarbonate, and extracted proteins were centrifuged at 14,000 x g to remove cellular debris and quantified by BCA assay (Thermo Scientific) according to the manufacturer's specifications. A total of 700 μg of protein extract from each sample was used for affinity purification of biotinylated proteins. First, cysteine disulfide bonds were reduced with 5 mM tris(2-carboxyethyl)phosphine (TCEP) at 30°C for 60 min followed by cysteine alkylation with 15 mM iodoacetamide (IAA) in the dark at room temperature for 30 min. Affinity purification was carried out in a Bravo AssayMap platform (Agilent) using AssayMap streptavidin cartridges (Agilent). Briefly, cartridges were first primed with 50 mM ammonium bicarbonate, and then proteins were slowly loaded onto the streptavidin cartridge. Background contamination was removed by extensively washing the cartridges with 8 M urea, 50 mM ammonium bicarbonate. Finally, cartridges were washed with Rapid digestion buffer (Promega, Rapid digestion buffer kit) and proteins were subjected to on-cartridge digestion with mass spec grade Trypsin/Lys-C Rapid digestion enzyme (Promega) at 70 ºC for 2 h. Digested peptides were then desalted in the Bravo platform using AssayMap C18 cartridges and the organic solvent was removed in a SpeedVac concentrator prior to LC-MS/MS analysis. Digested samples were analyzed on a Thermo Fisher Orbitrap Lumos mass spectrometer equipped with an Easy nLC 1200 ultra-high pressure liquid chromatography system. Samples were injected on an in-house packed C18 reverse phase column (25 cm x 75 μm packed with 1.7 μm, 130 Å pore size Bridged Ethylene Hybrid particles (Waters)). Peptides were separated by an organic gradient from 5% to 30% ACN in 0.1% formic acid over 130 minutes at a flow rate of 300 nL/min. The MS continuously acquired spectra in a data-dependent manner throughout the gradient, acquiring a full scan

in the Orbitrap (at 120,000 resolution with an AGC target of 1e6 and a maximum injection time of 100 ms) followed by as many MS/MS scans as could be acquired on the most abundant ions in 3 s in the Orbitrap (at 15,000 resolution, HCD collision energy of 30%, AGC target of 1e5, a maximum injection time of 22 ms, and an isolation width of 1.3 m/z). Singly and unassigned charge states were rejected. Dynamic exclusion was enabled with a repeat count of 1, an exclusion duration of 20 s, and an exclusion mass width of ± 10 ppm. Raw mass spectrometry data were processed using the MaxQuant software package and Andromeda search engine (version 1.5.5.1). Peptides were generated from a tryptic digestion of up to two missed cleavages and were searched against the Uniprot human protein database (downloaded on August 13, 2015). Variable modifications were allowed for N-terminal protein acetylation, methionine oxidation, and lysine acetylation. A static modification was indicated for carbamidomethyl cysteine. All other settings were left using MaxQuant default settings. Peptide and protein identifications were filtered to a 1% false discovery rate (FDR). Statistical analysis was performed using the MSstats software package.

Autophagy and LC3 flux Analysis—Macroautophagy activity in intact cells was measured upon transduction with lentivirus carrying the mCherry-GFP-LC3 tandem construct (Kimura et al., 2008). Cells were plated on coverslips or glass-bottom 96-well plates and fluorescence recorded from both channels. Puncta positive for both fluorophores correspond to autophagosomes whereas those only positive for the red fluorophore correspond to autolysosomes. Autophagic flux was determined as the conversion of autophagosomes (yellow) to autolysosomes (red puncta). Autophagy reporters were analyzed using high-content microscopy as follows: Cells plated in glass-bottom 96-well plates were treated for the indicated times and following fixation, images were acquired using a high-content microscope (Operetta, Perkin Elmer). Images of 9 different fields per well were captured resulting in an average of 2,500–3,000 cells. Nuclei and puncta were identified using the manufacturer's software. The number of particles/puncta per cell was quantified using the "particle identifier" function in the cytosolic region after thresholding in non-saturated images (Kaushik and Cuervo., 2009). In all cases, focal plane thickness was set at 0.17μm and sections with maximal nuclear diameter were selected for quantification. Values are presented as number of puncta per cell section, which represented 10–20% of the total puncta per cell. For LC3 flux analysis MODE-K cells were treated with lysosomal inhibitors (PI) (20 mM NH_4Cl and 200 μM leupeptin) for 0, 2 and 4 h. After the incubation, cells were lysed and subjected to immunoblotting analyses. Amount of LC3-II was normalized to that of actin. Net LC3 flux and autophagosome formation as $LC3II_{2h}$ - $LC3II_{0h}$ and $LC3II_{4h}$ - $LC3II_{2h}$, respectively.

Transmission electron microscopy and Morphometric analysis—MODE-K cells were fixed in glutaraldehyde. After embedding in Epon Araldite, sections were cut and examined using a Philips CM-100 Transmission Electron Microscope. Morphometric classification of autophagic vacuoles was done following the standard criteria (Singh et al., 2009) as follows: autophagosomes were distinguished as double membrane vesicles with content of similar density as the surrounding cytosol and comprised often of recognizable cellular structures; autophagolysosomes were identified as single or partially

double membrane vesicles of content of lower density than the surrounding cytosol and comprised of amorphous content or partially degraded cellular structures. In both cases, the limiting membrane had to be denuded of ribosomal particles. Multivesicular bodies were identified by the presence of luminal vesicles homogenous in size (<100nm). Amphisomes, corresponding to the fusion of autophagosomes with late endosomes/multivesicular bodies were identified by their single or partially double membrane, cytosolic cargo and presence of multivesicles of homogeneous size in the lumen. Morphometric analysis of autophagic compartments was done by double-blinded independent observers using a single-category allocation or each vesicle in at least 20 different micrographs per condition.

Immunoblotting Analysis—Cells for protein analysis were lysed in RIPA buffer (20 mM Tris-HCl, 37 mM NaCl2, 2 mM EDTA, 1% Triton-X, 10% glycerol, 0.1% SDS, and 0.5% sodium deoxycholate) with phosphatase and protease inhibitors. For immunoprecipitations, cells were lysed in IP lysis buffer (100 mM NaCl, 25 mM Tris, 1% Triton-X, 10% glycerol, with phosphatase and protease inhibitors) and immunoprecipitated with 25 μl of 50% slurry of protein Glutathione-Sepharose 4B beads (Bioworld). Immunoprecipitates were washed three times with lysis buffer, once with high salt (500 mM NaCl), and once more with lysis buffer. Protein concentration in lysates was determined by using Protein Assay Kit (Bio-Rad). Cell extracts and immunoprecipitated proteins were denatured, subjected to SDS-PAGE, transferred to PVDF membranes (GE Healthcare). After blocking with 5% nonfat dry milk in Tris-buffered saline and 0.1% Tween (TBS-T), the membranes were incubated with the specific antibodies (as listed in Key Resources Table) overnight at 4°C. After 2 h incubation with the appropriate horseradish peroxidase-conjugated antibodies, the immune complexes were detected by chemiluminescence (Thermo Scientific) or Near-infrared fluorescence (LI-COR).

In Vitro Phosphorylation—Fifteen μg of FLAG-tagged human ULK2 (FLAG-ULK2) or HA-tagged human TBK1 plasmid was transfected to ~80% confluent HEK293T cells in a P100 format. The amount of ULK2 mutants transfected were corrected to equal levels in the expression. Cells were lysed in RIPA buffer 48 h after transfection and HA-EZH2 was immunoprecipitated using anti-HA beads (Sigma) or anti-FLAG beads (Sigma). Immunoprecipitates were washed and incubated at 30ºC for 60 min in kinase-assay buffer containing 25 mM Tris-HCl (pH 7.5), 5 mM MgCl2, 0.5 mM EGTA, 1 mM DTT, and 400 μM ATPγS (Biolog) or 200 μM ATP in the presence of recombinant PKCλ/ι (Invitrogen) or recombinant ULK2 (Sigma). Detection of substrate phosphorylation was performed using the ATP analog-based phosphorylation detection used previously (Allen et al., 2007) with minor modifications. Briefly, after the phosphorylation reaction, PNBM (Abcam) and EDTA were added to a final concentration of 2.5 mM and 20 mM, respectively, and incubated for 1 h at room temperature. Immunoblotting detection was performed with anti-thiophosphate ester antibody (Abcam) or anti-phosphorylated TBK1 (Cell Signaling).

VECTRA Staining—Primary antibody dilutions were optimized individually at H220 retrieval using the Leica BondRx Automated IHC stainer and evaluated by a board-certified pathologist for specificity. Multiplexed staining was optimized then performed using the Automated Opal 7-Color IHC Kit (NEL821001KT) from Akoya Biosciences. A library for

spectral separation was generated by staining control tissue with each opal fluor conjugated to CD20. Slides were imaged in the Vectra Polaris Automated Quantitative Pathology Multispectral Imaging System. Exposure times were maximized under the constraint that no pixel saturate the detector (Patel and Rodig, 2020; Patel et al., 2019).

Computational Analysis of VECTRA Images—All TMA cores were processed by linear spectral unmixing and deconvolved (Parra et al., 2017). Regions for visualization were manually selected and appropriately preprocessed for display using the open-source Fiji distribution of ImageJ (Schindelin et al., 2012). Cells were segmented using the pretrained Mesmer deep learning model based on the ResNet50 architecture and panoptic feature pyramid(https://www.biorxiv.org/content/10.1101/2021.03.01.431313v1.full.pdf, https://www.cvfoundation.org/openaccess/content_cvpr_2016/papers/He_Deep_Residual_Learning_CVPR_2016_paper.pdf). All fluorescent channels were then quantified using the segmentation mask to generate a counts matrix representing the average expression of each marker in each cell (van der Walt et al., 2014). DAPI negative cells were filtered as artifacts. A 15-nearest-neighbor graph was generated from the counts matrix using Euclidean metric as implemented in the Scanpy python package (Wolf et al., 2018), and clustered using the Leiden algorithm (Traag et al., 2019) to identify putative subpopulations of cells and identify low-quality cells. Cells were projected to two dimensions and visualized using the Uniform Manifold Approximation and Projection algorithm (UMAP) (https://arxiv.org/abs/1802.03426). Cells were phenotyped by thresholding markers for positive or negative signal with pathologist assistance. Differential expression analysis was implemented by Wilcoxon test. Spatial enrichment was computed by permutation test, and differential spatial enrichment was tested by rank-sum Wilcoxon test.

RNA extraction and analysis—Total RNA from mouse tissues, cells and cultured organoids was extracted using the TRIZOL reagent (Invitrogen) and the RNeasy Mini Kit (QIAGEN), followed by DNase treatment. After quantification using a Nanodrop 1000 spectrophotometer (Thermo Scientific), RNA was either processed for RNA-seq or reverse-transcribed using random primers and MultiScribe Reverse Transcriptase (Applied Biosystems). Gene expression was analyzed by amplifying 20 ng of the complementary DNA using the CFX96 Real Time PCR Detection System with SYBR Green Master Mix (BioRad) and primers described in Table S1. The amplification parameters were set at 95°C for 30 s, 58°C for 30 s, and 72°C for 30 s (40 cycles total). Gene expression values for each sample were normalized to the 18s RNA.

3’ RNA-seq Preparation and Sequencing—Total RNA from MTOs was extracted using Quick-RNA MiniPrep kit (Zymo Research). Libraries were prepared from 200 ng of total RNA using the QuantSeq 3’ mRNA-Seq Library Prep Kit FWD for Illumina from Lexogen, and optional UMIs (Vienna, Austria). Barcoded libraries were pooled, and single end sequenced (1X75) on the Illumina NextSeq 500 using the High output V2.5 kit (Illumina Inc., San Diego CA).

ATAC-Seq Library Preparation and Sequencing—The cell pellet was resuspended in 50 μl lysis buffer and then spun down 500 × g for 10 min at 4°C. The nuclei pellet was resuspended into 50 μl transposition reaction mixture containing Tn5 transposase from Nextera DNA Library Prep Kit (Illumina) and incubated at 37°C for 30 min. Then the transposase-associated DNA was purified using MinElute PCR purification kit (QIAGEN). To amplify the library, the DNA was first amplified for 5 cycles using indexing primer from Nextera kit and NEBNext High-Fidelity 2X PCR master mix. To reduce the PCR amplification bias, 5 μl of amplified DNA after the first 5 cycles was used to do qPCR of 20 cycles to decide the number of cycles for the second round of PCR. Usually, the maximum cycle of the second round of PCR is 5 cycles. Then the total amplified DNA was size selected to fragments less than 800 bp using SPRI beads. Quantification of the ATAC-seq library was done with QuBit. The size of the pooled library was examined by TapeStation. Barcoded ATAC-seq libraries were pooled and paired end sequenced (sX75) on the Illumina NextSeq 500 using the High output V2.5 kit (Illumina Inc., San Diego, CA)

Bioinformatics Analysis—For RNA-Seq, sequencing Fastq files were uploaded to BaseSpace and processed with RNA-Seq Alignment App (Illumina) to obtain raw reads counts for each gene. For 3'RNA-Seq, read data was processed with the BlueBee Genomics Platform (BlueBee, San Mateo, CA). GenePattern (https://genepattern.broadinstitute.org/gp/pages/index.jsf) was used to collapse gene matrix files (CollapseDataset module) or to assess the statistical significance of differential gene expression (ComparativeMarkerSelection module for microarray data and DESeq2 module for RNA-seq data). Heat-map representation of gene expression was generated using Morpheus (https://software.broadinstitute.org/morpheus/). Gene Set Enrichment Analysis (GSEA) was performed using GSEA v4.1.0 software (http://www.broadinstitute.org/gsea/index.jsp) with 1000 gene-set permutations using the gene-ranking metric T-test with the MSigDb collections for customized signatures. In order to explore autophagy associated genes signature, we customized "Autophagy-lysosome signature" as described (Perera et al., 2015). PageRank analysis combining ATAC-Seq and RNA-Seq was performed with Taiji v1.1.0 (Zhang et al., 2019).

Bioinformatics Analysis of clinical data—Raw gene expression data from inflammatory bowel disease (IBD) samples datasets (GSE36807, GSE59071, GSE10616, GSE10714, GSE48959, GSE9452, GSE16879, and GSE23597) were directly accessed through the GEO (https://www.ncbi.nlm.nih.gov/geo/). Data for TCGA-COREAD was accessed through cBioportal (http://www.cbioportal.org/index.do). Gene matrix files were modified to comply with .gct file format and used as input file for Gene Set Enrichment Analysis (GSEA). GSEA was performed using GSEA v4.1.0 module on GenePattern (https://cloud.genepattern.org/, Broad Institute) with 1,000 gene-set permutations using the gene ranking metric tTest or with MSigDb collections or customized genesets. TCGA patients (n=383) were classified in *PRKCI*^{high} or *PRKCI*^{low} based on *PRKCI* expression using z-score. For survival analysis, the cut-off values were evaluated based on the association between patient survival and gene expression using the Survminer R package. Interferon score was calculated using the 82-gene Hallmark_Interferon_Alpha_response signature (MSigDb) and the gene set variation analysis (GSVA) algorithm. Single-cell

RNA-seq data of CRC patients were obtained from GSE132465. Filtered count matrix were imported to R to further analysis using the Seurat package (Stuart et al., 2019). Dimensionality reduction was performed by principal component analysis and UMAP embedding with 30 principal components and resolution 0.5. Clusters were then annotated based on original deposited metadata. *PRKCI* expression in tumor epithelial cells were obtained using the "AverageExpression" function in Seurat. Patients were then classified in $PRKCI^{high}$ or $PRKCI^{low}$ as above. Expression scores of the selected signatures were calculated for each individual cell using the "AddModuleScore" Seurat function.

Quantification and Statistical Analysis—All the statistical tests were justified for every figure. All samples represent biological replicates. Data are presented as the mean ± SEM. Statistical analysis was performed using GraphPad Prism 8 or R software environment (http://www.r-project.org/). Significant differences between groups were determined using a Student's t-test (two-tailed) when the data met the normal distribution tested by D'Agostino test. If the data did not meet this test, a Mann-Whitney *U*-test was used. Differences between more than 3 groups were determined using one-way ANOVA test (parametric) or Brown-Forsythe and Welch ANOVA tests (nonparametric) followed by Dunnett post hoc test. If the data did not meet this test, a Mann-Whitney test was used. Differences in Kaplan Meier plots were analyzed by Gehan-Breslow-Wilcoxon test. The chi-square test or Fisher's exact test was used to determine the significance of differences between covariates. Logistic regression analysis was employed to estimate univariate and multivariate odds ratio and 95% confidence interval (CI). Values of $p < 0.05$ were considered as significantly different.

Supplementary Material

Refer to Web version on PubMed Central for supplementary material.

ACKNOWLEDGMENTS

Research was supported by grants by NCI of the National Institutes of Health under awards numbers: R01CA207177 and R01CA250025 to J.M; R01CA218254 to M.T.D.-M; P50CA211024 to M.L. Project support for this research was provided in part by the Center for Translational Pathology and the Multiparametric In Situ Imaging Laboratory in the Department of Pathology and Laboratory Medicine, Weill Cornell Medicine. We thank Dr. Eduard Batlle (IRB Barcelona, Spain) for generously providing MTO organoids. We thank Tavonna Bryant and Tararin Nikomborirak for technical assistance. J.M. and M.T.D.-M. are Homer T. Hirst III Professors of Oncology in Pathology.

REFERENCES

Allen JJ, Li M, Brinkworth CS, Paulson JL, Wang D, Hubner A, Chou WH, Davis RJ, Burlingame AL, Messing RO, et al. (2007). A semisynthetic epitope for kinase substrates. Nat Methods 4, 511–516. [PubMed: 17486086]

Arijs I, De Hertogh G, Lemaire K, Quintens R, Van Lommel L, Van Steen K, Leemans P, Cleynen I, Van Assche G, Vermeire S, et al. (2009). Mucosal gene expression of antimicrobial peptides in inflammatory bowel disease before and after first infliximab treatment. PLoS One 4, e7984. [PubMed: 19956723]

Barber DL, Wherry EJ, Masopust D, Zhu B, Allison JP, Sharpe AH, Freeman GJ, and Ahmed R. (2006). Restoring function in exhausted CD8 T cells during chronic viral infection. Nature 439, 682–687. [PubMed: 16382236]

Benci JL, Xu B, Qiu Y, Wu TJ, Dada H, Twyman-Saint Victor C, Cucolo L, Lee DSM, Pauken KE, Huang AC, et al. (2016). Tumor Interferon Signaling Regulates a Multigenic Resistance Program to Immune Checkpoint Blockade. Cell 167, 1540–1554 e1512. [PubMed: 27912061]

Bezu L, Gomes-de-Silva LC, Dewitte H, Breckpot K, Fucikova J, Spisek R, Galluzzi L, Kepp O, and Kroemer G. (2015). Combinatorial strategies for the induction of immunogenic cell death. Front Immunol 6, 187. [PubMed: 25964783]

Bruni D, Angell HK, and Galon J. (2020). The immune contexture and Immunoscore in cancer prognosis and therapeutic efficacy. Nat Rev Cancer 20, 662–680. [PubMed: 32753728]

Burdette DL, and Vance RE (2013). STING and the innate immune response to nucleic acids in the cytosol. Nat Immunol 14, 19–26. [PubMed: 23238760]

Calon A, Lonardo E, Berenguer-Llergo A, Espinet E, Hernando-Momblona X, Iglesias M, Sevillano M, Palomo-Ponce S, Tauriello DV, Byrom D, et al. (2015). Stromal gene expression defines poor-prognosis subtypes in colorectal cancer. Nat Genet 47, 320–329. [PubMed: 25706628]

Ciechanover A. (2015). The unravelling of the ubiquitin system. Nat Rev Mol Cell Biol 16, 322–324. [PubMed: 25907614]

De Sousa EMF, Wang X, Jansen M, Fessler E, Trinh A, de Rooij LP, de Jong JH, de Boer OJ, van Leersum R, Bijlsma MF, et al. (2013). Poor-prognosis colon cancer is defined by a molecularly distinct subtype and develops from serrated precursor lesions. Nat Med 19, 614–618. [PubMed: 23584090]

Dersh D, Holly J, and Yewdell JW (2021). A few good peptides: MHC class I-based cancer immunosurveillance and immunoevasion. Nat Rev Immunol 21, 116–128. [PubMed: 32820267]

Duran A, Amanchy R, Linares JF, Joshi J, Abu-Baker S, Porollo A, Hansen M, Moscat J, and Diaz-Meco MT (2011). p62 is a key regulator of nutrient sensing in the mTORC1 pathway. Mol Cell 44, 134–146. [PubMed: 21981924]

Egan DF, Chun MG, Vamos M, Zou H, Rong J, Miller CJ, Lou HJ, Raveendra-Panickar D, Yang CC, Sheffler DJ, et al. (2015). Small Molecule Inhibition of the Autophagy Kinase ULK1 and Identification of ULK1 Substrates. Mol Cell 59, 285–297. [PubMed: 26118643]

el Marjou F, Janssen KP, Chang BH, Li M, Hindie V, Chan L, Louvard D, Chambon P, Metzger D, and Robine S. (2004). Tissue-specific and inducible Cre-mediated recombination in the gut epithelium. Genesis 39, 186–193. [PubMed: 15282745]

Galluzzi L, Bravo-San Pedro JM, Demaria S, Formenti SC, and Kroemer G. (2017). Activating autophagy to potentiate immunogenic chemotherapy and radiation therapy. Nat Rev Clin Oncol 14, 247–258. [PubMed: 27845767]

Galon J, Costes A, Sanchez-Cabo F, Kirilovsky A, Mlecnik B, Lagorce-Pages C, Tosolini M, Camus M, Berger A, Wind P, et al. (2006). Type, density, and location of immune cells within human colorectal tumors predict clinical outcome. Science 313, 1960–1964. [PubMed: 17008531]

Gao J, Shi LZ, Zhao H, Chen J, Xiong L, He Q, Chen T, Roszik J, Bernatchez C, Woodman SE, et al. (2016). Loss of IFN-gamma Pathway Genes in Tumor Cells as a Mechanism of Resistance to Anti-CTLA-4 Therapy. Cell 167, 397–404 e399. [PubMed: 27667683]

Gentles AJ, Newman AM, Liu CL, Bratman SV, Feng W, Kim D, Nair VS, Xu Y, Khuong A, Hoang CD, et al. (2015). The prognostic landscape of genes and infiltrating immune cells across human cancers. Nat Med 21, 938–945. [PubMed: 26193342]

Germano G, Lamba S, Rospo G, Barault L, Magri A, Maione F, Russo M, Crisafulli G, Bartolini A, Lerda G, et al. (2017). Inactivation of DNA repair triggers neoantigen generation and impairs tumour growth. Nature 552, 116–120. [PubMed: 29186113]

Guinney J, Dienstmann R, Wang X, de Reynies A, Schlicker A, Soneson C, Marisa L, Roepman P, Nyamundanda G, Angelino P, et al. (2015). The consensus molecular subtypes of colorectal cancer. Nat Med 21, 1350–1356. [PubMed: 26457759]

Hanzelmann S, Castelo R, and Guinney J. (2013). GSVA: gene set variation analysis for microarray and RNA-seq data. BMC Bioinformatics 14, 7. [PubMed: 23323831]

Hopfner KP, and Hornung V. (2020). Molecular mechanisms and cellular functions of cGAS-STING signalling. Nat Rev Mol Cell Biol 21, 501–521. [PubMed: 32424334]

Hu MM, Yang Q, Xie XQ, Liao CY, Lin H, Liu TT, Yin L, and Shu HB (2016). Sumoylation Promotes the Stability of the DNA Sensor cGAS and the Adaptor STING to Regulate the Kinetics of Response to DNA Virus. Immunity 45, 555–569. [PubMed: 27637147]

Huang X, Chen J, Cao W, Yang L, Chen Q, He J, Yi Q, Huang H, Zhang E, and Cai Z. (2019). The many substrates and functions of NEDD4–1. Cell Death Dis 10, 904. [PubMed: 31787758]

Ishikawa H, and Barber GN (2008). STING is an endoplasmic reticulum adaptor that facilitates innate immune signalling. Nature 455, 674–678. [PubMed: 18724357]

Jones S, Chen WD, Parmigiani G, Diehl F, Beerenwinkel N, Antal T, Traulsen A, Nowak MA, Siegel C, Velculescu VE, et al. (2008). Comparative lesion sequencing provides insights into tumor evolution. Proc Natl Acad Sci U S A 105, 4283–4288. [PubMed: 18337506]

Kasashima H, Duran A, Martinez-Ordonez A, Nakanishi Y, Kinoshita H, Linares JF, Reina-Campos M, Kudo Y, L'Hermitte A, Yashiro M, et al. (2020). Stromal SOX2 Upregulation Promotes Tumorigenesis through the Generation of a SFRP1/2-Expressing Cancer-Associated Fibroblast Population. Dev Cell.

Kimura S, Noda T, and Yoshimori T. (2008). Dynein-dependent movement of autophagosomes mediates efficient encounters with lysosomes. Cell Struct Funct 33, 109–122. [PubMed: 18388399]

Kudo Y, Sugimoto M, Arias E, Kasashima H, Cordes T, Linares JF, Duran A, Nakanishi Y, Nakanishi N, L'Hermitte A, et al. (2020). PKClambda/iota Loss Induces Autophagy, Oxidative Phosphorylation, and NRF2 to Promote Liver Cancer Progression. Cancer Cell 38, 247–262 e211. [PubMed: 32589943]

Kugathasan S, Baldassano RN, Bradfield JP, Sleiman PM, Imielinski M, Guthery SL, Cucchiara S, Kim CE, Frackelton EC, Annaiah K, et al. (2008). Loci on 20q13 and 21q22 are associated with pediatric-onset inflammatory bowel disease. Nat Genet 40, 1211–1215. [PubMed: 18758464]

Langmead B, and Salzberg SL (2012). Fast gapped-read alignment with Bowtie 2. Nat Methods 9, 357–359. [PubMed: 22388286]

Le DT, Durham JN, Smith KN, Wang H, Bartlett BR, Aulakh LK, Lu S, Kemberling H, Wilt C, Luber BS, et al. (2017). Mismatch repair deficiency predicts response of solid tumors to PD-1 blockade. Science 357, 409–413. [PubMed: 28596308]

Lee HO, Hong Y, Etlioglu HE, Cho YB, Pomella V, Van den Bosch B, Vanhecke J, Verbandt S, Hong H, Min JW, et al. (2020). Lineage-dependent gene expression programs influence the immune landscape of colorectal cancer. Nat Genet 52, 594–603. [PubMed: 32451460]

Lee EJ, and Tournier C. (2011). The requirement of uncoordinated 51-like kinase 1 (ULK1) and ULK2 in the regulation of autophagy. Autophagy 7, 689–695. [PubMed: 21460635]

Leitges M, Sanz L, Martin P, Duran A, Braun U, Garcia JF, Camacho F, Diaz-Meco MT, Rennert PD, and Moscat J. (2001). Targeted disruption of the zetaPKC gene results in the impairment of the NF-kappaB pathway. Molecular cell 8, 771–780. [PubMed: 11684013]

Liao W, Overman MJ, Boutin AT, Shang X, Zhao D, Dey P, Li J, Wang G, Lan Z, Li J, et al. (2019). KRAS-IRF2 Axis Drives Immune Suppression and Immune Therapy Resistance in Colorectal Cancer. Cancer Cell 35, 559–572 e557. [PubMed: 30905761]

Linares JF, Duran A, Reina-Campos M, Aza-Blanc P, Campos A, Moscat J, and Diaz-Meco MT (2015). Amino Acid Activation of mTORC1 by a PB1-Domain-Driven Kinase Complex Cascade. Cell Rep.

Linares JF, Duran A, Yajima T, Pasparakis M, Moscat J, and Diaz-Meco MT (2013). K63 polyubiquitination and activation of mTOR by the p62-TRAF6 complex in nutrient-activated cells. Mol Cell 51, 283–296. [PubMed: 23911927]

Madison BB, Dunbar L, Qiao XT, Braunstein K, Braunstein E, and Gumucio DL (2002). Cis elements of the villin gene control expression in restricted domains of the vertical (crypt) and horizontal (duodenum, cecum) axes of the intestine. J Biol Chem 277, 33275–33283. [PubMed: 12065599]

Mandal R, Samstein RM, Lee KW, Havel JJ, Wang H, Krishna C, Sabio EY, Makarov V, Kuo F, Blecua P, et al. (2019). Genetic diversity of tumors with mismatch repair deficiency influences anti-PD-1 immunotherapy response. Science 364, 485–491. [PubMed: 31048490]

Martini G, Dienstmann R, Ros J, Baraibar I, Cuadra-Urteaga JL, Salva F, Ciardiello D, Mulet N, Argiles G, Tabernero J, et al. (2020). Molecular subtypes and the evolution of treatment management in metastatic colorectal cancer. Ther Adv Med Oncol 12, 1758835920936089.

Massey AC, Kaushik S, Sovak G, Kiffin R, and Cuervo AM (2006). Consequences of the selective blockage of chaperone-mediated autophagy. Proc Natl Acad Sci U S A 103, 5805–5810. [PubMed: 16585521]

Mlecnik B, Bindea G, Kirilovsky A, Angell HK, Obenauf AC, Tosolini M, Church SE, Maby P, Vasaturo A, Angelova M, et al. (2016). The tumor microenvironment and Immunoscore are critical determinants of dissemination to distant metastasis. Science translational medicine 8, 327ra326.

Montero-Melendez T, Llor X, Garcia-Planella E, Perretti M, and Suarez A. (2013). Identification of novel predictor classifiers for inflammatory bowel disease by gene expression profiling. PLoS One 8, e76235. [PubMed: 24155895]

Moscat J, and Diaz-Meco MT (2020). The interplay between PRKCI/PKClambda/iota, SQSTM1/p62, and autophagy orchestrates the oxidative metabolic response that drives liver cancer. Autophagy 16, 1915–1917. [PubMed: 32686580]

Moscat J, Karin M, and Diaz-Meco MT (2016). p62 in Cancer: Signaling Adaptor Beyond Autophagy. Cell 167, 606–609. [PubMed: 27768885]

Nakanishi Y, Duran A, L'Hermitte A, Shelton PM, Nakanishi N, Reina-Campos M, Huang J, Soldevila F, Baaten BJG, Tauriello DVF, et al. (2018). Simultaneous Loss of Both Atypical Protein Kinase C Genes in the Intestinal Epithelium Drives Serrated Intestinal Cancer by Impairing Immunosurveillance. Immunity 49, 1132–1147 e1137. [PubMed: 30552022]

Nakanishi Y, Reina-Campos M, Nakanishi N, Llado V, Elmen L, Peterson S, Campos A, De SK, Leitges M, Ikeuchi H, et al. (2016). Control of Paneth Cell Fate, Intestinal Inflammation, and Tumorigenesis by PKClambda/iota. Cell Rep 16, 3297–3310. [PubMed: 27653691]

Olsen J, Gerds TA, Seidelin JB, Csillag C, Bjerrum JT, Troelsen JT, and Nielsen OH (2009). Diagnosis of ulcerative colitis before onset of inflammation by multivariate modeling of genome-wide gene expression data. Inflamm Bowel Dis 15, 1032–1038. [PubMed: 19177426]

Overman MJ, McDermott R, Leach JL, Lonardi S, Lenz HJ, Morse MA, Desai J, Hill A, Axelson M, Moss RA, et al. (2017). Nivolumab in patients with metastatic DNA mismatch repair-deficient or microsatellite instability-high colorectal cancer (CheckMate 142): an open-label, multicentre, phase 2 study. Lancet Oncol 18, 1182–1191. [PubMed: 28734759]

Parra ER, Uraoka N, Jiang M, Cook P, Gibbons D, Forget MA, Bernatchez C, Haymaker C, Wistuba II, and Rodriguez-Canales J. (2017). Validation of multiplex immunofluorescence panels using multispectral microscopy for immune-profiling of formalin-fixed and paraffin-embedded human tumor tissues. Sci Rep 7, 13380. [PubMed: 29042640]

Patel SS, and Rodig SJ (2020). Overview of Tissue Imaging Methods. Methods Mol Biol 2055, 455–465. [PubMed: 31502165]

Patel SS, Weirather JL, Lipschitz M, Lako A, Chen PH, Griffin GK, Armand P, Shipp MA, and Rodig SJ (2019). The microenvironmental niche in classic Hodgkin lymphoma is enriched for CTLA-4-positive T cells that are PD-1-negative. Blood 134, 2059–2069. [PubMed: 31697809]

Pejaver V, Urresti J, Lugo-Martinez J, Pagel KA, Lin GN, Nam HJ, Mort M, Cooper DN, Sebat J, Iakoucheva LM, et al. (2020). Inferring the molecular and phenotypic impact of amino acid variants with MutPred2. Nat Commun 11, 5918. [PubMed: 33219223]

Perera RM, Stoykova S, Nicolay BN, Ross KN, Fitamant J, Boukhali M, Lengrand J, Deshpande V, Selig MK, Ferrone CR, et al. (2015). Transcriptional control of autophagy-lysosome function drives pancreatic cancer metabolism. Nature 524, 361–365. [PubMed: 26168401]

Poillet-Perez L, Sharp DW, Yang Y, Laddha SV, Ibrahim M, Bommareddy PK, Hu ZS, Vieth J, Haas M, Bosenberg MW, et al. (2020). Autophagy promotes growth of tumors with high mutational burden by inhibiting a T-cell immune response. Nature Cancer 1, 923–934. [PubMed: 34476408]

Putz U, Howitt J, Lackovic J, Foot N, Kumar S, Silke J, and Tan SS (2008). Nedd4 family-interacting protein 1 (Ndfip1) is required for the exosomal secretion of Nedd4 family proteins. J Biol Chem 283, 32621–32627. [PubMed: 18819914]

Qiu WR, Xiao X, Lin WZ, and Chou KC (2015). iUbiq-Lys: prediction of lysine ubiquitination sites in proteins by extracting sequence evolution information via a gray system model. J Biomol Struct Dyn 33, 1731–1742. [PubMed: 25248923]

Reina-Campos M, Diaz-Meco MT, and Moscat J. (2019a). The Dual Roles of the Atypical Protein Kinase Cs in Cancer. Cancer Cell 36, 218–235. [PubMed: 31474570]

Reina-Campos M, Linares JF, Duran A, Cordes T, L'Hermitte A, Badur MG, Bhangoo MS, Thorson PK, Richards A, Rooslid T, et al. (2019b). Increased Serine and One-Carbon Pathway Metabolism by PKClambda/iota Deficiency Promotes Neuroendocrine Prostate Cancer. Cancer Cell 35, 385–400 e389. [PubMed: 30827887]

Saleiro D, Mehrotra S, Kroczynska B, Beauchamp EM, Lisowski P, Majchrzak-Kita B, Bhagat TD, Stein BL, McMahon B, Altman JK, et al. (2015). Central role of ULK1 in type I interferon signaling. Cell Rep 11, 605–617. [PubMed: 25892232]

Samie M, Lim J, Verschueren E, Baughman JM, Peng I, Wong A, Kwon Y, Senbabaoglu Y, Hackney JA, Keir M, et al. (2018). Selective autophagy of the adaptor TRIF regulates innate inflammatory signaling. Nat Immunol 19, 246–254. [PubMed: 29358708]

Sanchez P, De Carcer G, Sandoval IV, Moscat J, and Diaz-Meco MT (1998). Localization of atypical protein kinase C isoforms into lysosome-targeted endosomes through interaction with p62. Mol Cell Biol 18, 3069–3080. [PubMed: 9566925]

Schindelin J, Arganda-Carreras I, Frise E, Kaynig V, Longair M, Pietzsch T, Preibisch S, Rueden C, Saalfeld S, Schmid B, et al. (2012). Fiji: an open-source platform for biological-image analysis. Nat Methods 9, 676–682. [PubMed: 22743772]

Siegel RL, Miller KD, Fedewa SA, Ahnen DJ, Meester RGS, Barzi A, and Jemal A. (2017). Colorectal cancer statistics, 2017. CA Cancer J Clin 67, 177–193. [PubMed: 28248415]

Singh R, Kaushik S, Wang Y, Xiang Y, Novak I, Komatsu M, Tanaka K, Cuervo AM, and Czaja MJ (2009). Autophagy regulates lipid metabolism. Nature 458, 1131–1135. [PubMed: 19339967]

Stuart T, Butler A, Hoffman P, Hafemeister C, Papalexi E, Mauck WM 3rd, Hao Y, Stoeckius M, Smibert P, and Satija R. (2019). Comprehensive Integration of Single-Cell Data. Cell 177, 1888–1902 e1821. [PubMed: 31178118]

Sun L, Wu J, Du F, Chen X, and Chen ZJ (2013). Cyclic GMP-AMP synthase is a cytosolic DNA sensor that activates the type I interferon pathway. Science 339, 786–791. [PubMed: 23258413]

Tauriello DVF, Palomo-Ponce S, Stork D, Berenguer-Llergo A, Badia-Ramentol J, Iglesias M, Sevillano M, Ibiza S, Canellas A, Hernando-Momblona X, et al. (2018). TGFbeta drives immune evasion in genetically reconstituted colon cancer metastasis. Nature 554, 538–543. [PubMed: 29443964]

Toedter G, Li K, Marano C, Ma K, Sague S, Huang CC, Song XY, Rutgeerts P, and Baribaud F. (2011). Gene expression profiling and response signatures associated with differential responses to infliximab treatment in ulcerative colitis. Am J Gastroenterol 106, 1272–1280. [PubMed: 21448149]

Tosolini M, Kirilovsky A, Mlecnik B, Fredriksen T, Mauger S, Bindea G, Berger A, Bruneval P, Fridman WH, Pages F, et al. (2011). Clinical impact of different classes of infiltrating T cytotoxic and helper cells (Th1, th2, treg, th17) in patients with colorectal cancer. Cancer Res 71, 1263–1271. [PubMed: 21303976]

Traag VA, Waltman L, and van Eck NJ (2019). From Louvain to Leiden: guaranteeing well-connected communities. Sci Rep 9, 5233. [PubMed: 30914743]

Van der Goten J, Vanhove W, Lemaire K, Van Lommel L, Machiels K, Wollants WJ, De Preter V, De Hertogh G, Ferrante M, Van Assche G, et al. (2014). Integrated miRNA and mRNA expression profiling in inflamed colon of patients with ulcerative colitis. PLoS One 9, e116117. [PubMed: 25546151]

van der Walt S, Schonberger JL, Nunez-Iglesias J, Boulogne F, Warner JD, Yager N, Gouillart E, Yu T, and scikit-image, c. (2014). scikit-image: image processing in Python. PeerJ 2, e453. [PubMed: 25024921]

Vanhove W, Peeters PM, Staelens D, Schraenen A, Van der Goten J, Cleynen I, De Schepper S, Van Lommel L, Reynaert NL, Schuit F, et al. (2015). Strong Upregulation of AIM2 and IFI16

Inflammasomes in the Mucosa of Patients with Active Inflammatory Bowel Disease. Inflamm Bowel Dis 21, 2673–2682. [PubMed: 26313692]

Vitale I, Shema E, Loi S, and Galluzzi L. (2021). Intratumoral heterogeneity in cancer progression and response to immunotherapy. Nat Med 27, 212–224. [PubMed: 33574607]

Wolf FA, Angerer P, and Theis FJ (2018). SCANPY: large-scale single-cell gene expression data analysis. Genome Biol 19, 15. [PubMed: 29409532]

Yamamoto K, Venida A, Yano J, Biancur DE, Kakiuchi M, Gupta S, Sohn ASW, Mukhopadhyay S, Lin EY, Parker SJ, et al. (2020). Autophagy promotes immune evasion of pancreatic cancer by degrading MHC-I. Nature 581, 100–105. [PubMed: 32376951]

Yamazaki T, Kirchmair A, Sato A, Buque A, Rybstein M, Petroni G, Bloy N, Finotello F, Stafford L, Navarro Manzano E, et al. (2020). Mitochondrial DNA drives abscopal responses to radiation that are inhibited by autophagy. Nat Immunol 21, 1160–1171. [PubMed: 32747819]

Zaretsky JM, Garcia-Diaz A, Shin DS, Escuin-Ordinas H, Hugo W, Hu-Lieskovan S, Torrejon DY, Abril-Rodriguez G, Sandoval S, Barthly L, et al. (2016). Mutations Associated with Acquired Resistance to PD-1 Blockade in Melanoma. N Engl J Med 375, 819–829. [PubMed: 27433843]

Zhang K, Wang M, Zhao Y, and Wang W. (2019). Taiji: System-level identification of key transcription factors reveals transcriptional waves in mouse embryonic development. Sci Adv 5, eaav3262. [PubMed: 30944857]

Zhang Y, Yeruva L, Marinov A, Prantner D, Wyrick PB, Lupashin V, and Nagarajan UM (2014). The DNA sensor, cyclic GMP-AMP synthase, is essential for induction of IFN-beta during Chlamydia trachomatis infection. J Immunol 193, 2394–2404. [PubMed: 25070851]

Zhao P, Wong KI, Sun X, Reilly SM, Uhm M, Liao Z, Skorobogatko Y, and Saltiel AR (2018). TBK1 at the Crossroads of Inflammation and Energy Homeostasis in Adipose Tissue. Cell 172, 731–743 e712. [PubMed: 29425491]

Zhong Z, Sanchez-Lopez E, and Karin M. (2016). Autophagy, Inflammation, and Immunity: A Troika Governing Cancer and Its Treatment. Cell 166, 288–298. [PubMed: 27419869]

Highlights

- Low PKCλ/ι levels correlate with enhanced IFN signaling and good prognosis in CRC
- PKCλ/ι loss inhibits intestinal tumorigenesis through IFN and $CD8^+$ T cell recruitment
- PKCλ/ι inactivation selectively stimulates ULK2 to promote TBK1-STING-IRF3 signaling
- Macroautophagy activation by PKCλ/ι loss prevents CMA-dependent degradation of STING

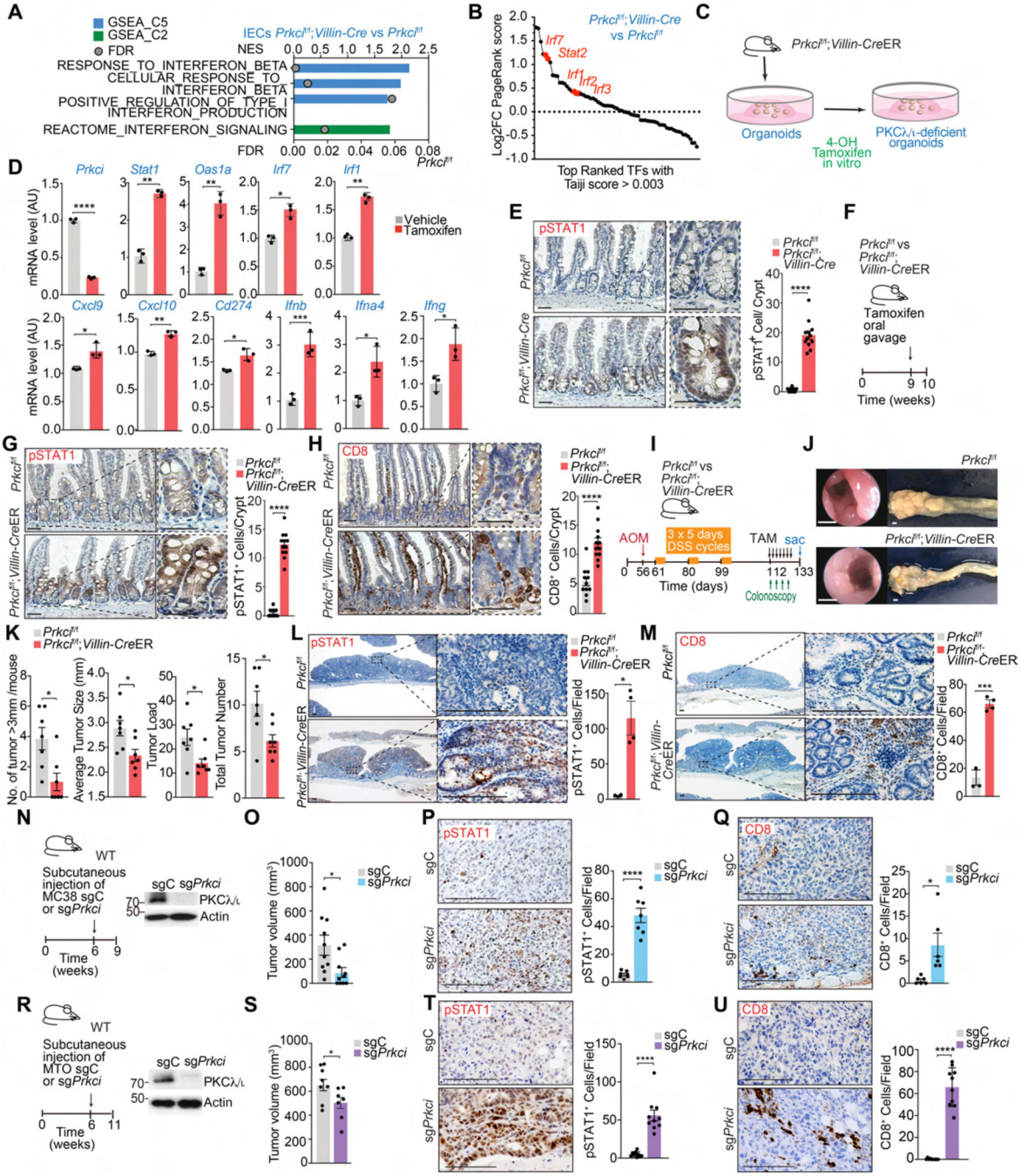

Figure 1. PKCλ/ι deficiency results in the upregulation of the IFN pathway in intestinal epithelial cells

(A) GSEA of transcriptomic data from RNA-seq on *Prkci*$^{f/f}$;*Villin-Cre* versus *Prkci*$^{f/f}$ IECs using compilation C5 and C2 (MSigDB).

(B) Scatterplot of mRNA expression and PageRank *Z* score for transcription factor genes upregulated in *Prkci*$^{f/f}$;*Villin-Cre* IECS.

(C) Schematic representation for tamoxifen treatment in organoids from *Prkci*$^{f/f}$;*Villin-CreER* mice. Organoids were stimulated with 500 nM of tamoxifen or vehicle for 3 days.

(D) qRT-PCR analysis of mRNA levels of IFN-related genes in tamoxifen-treated organoids and non-treated organoids from *Prkci*$^{f/f}$;*Villin-Cre*ER mice.
(E) pSTAT1 staining and quantification in small intestines from *Prkci*$^{f/f}$;*Villin-Cre* (n = 4) and *Prkci*$^{f/f}$ (n = 4) mice. Scale bar, 50 μm.
(F) Schematic representation for tamoxifen treatment in *Prkci*$^{f/f}$;*Villin-Cre*ER mice. Tamoxifen was injected by oral gavage (240 mg/kg) and mice were sacrificed after 7 days treatment.
(G and H) pSTAT1 (G) or CD8 (H) staining and quantification of small intestines from *Prkci*$^{f/f}$;*Villin-Cre* (n = 3) and *Prkci*$^{f/f}$ (n = 3) mice treated as in (F). Scale bar, 50 μm.
(I-M) *Prkci*$^{f/f}$ (n = 3) and *Prkci*$^{f/f}$;*Villin-Cre*ER (n = 4) mice treated with the azoxymethane (AOM)/DSS protocol and tamoxifen treatment. Experimental design (I), macroscopic images (J), quantification of the tumor number, tumor size and tumor load (K), pSTAT1 (L), CD8 (M) staining and quantification of colon tumors from *Prkci*$^{f/f}$;*Villin-Cre* and *Prkci*$^{f/f}$ mice treated as in (I). Scale bars, 1 mm (J), 50 μm L), and (M).
(N-Q) Subcutaneous injection of sg*Prkci* (n = 5) and sgC (n = 5) MC38 cells in WT mice. Experimental design and immunoblot analysis of indicated proteins in sg*Prkci* and sgC MC38 cells (N), quantification of the tumor volume (O), pSTAT1 (P) and CD8 (Q) staining and quantification from tumors originated from sg*Prkci* and sgC MC38 cells. Scale bar, 100 μm. (R-U) Subcutaneous injection of sg*Prkci* (n = 5) and sgC (n = 5) mouse tumor organoids (MTOs) in WT mice. Experimental design and immunoblot analysis of indicated proteins in sg*Prkci* and sgC MTOs (R), quantification of the tumor volume (S), pSTAT1 (T) and CD8 (U) staining and quantification from tumors originated from sg*Prkci* and sgC MTOs. Scale bar, 50 μm.
Results are shown as mean ± SEM *p < 0.05, **p < 0.01, ***p < 0.001, ****p < 0.0001. See also Figure S1.

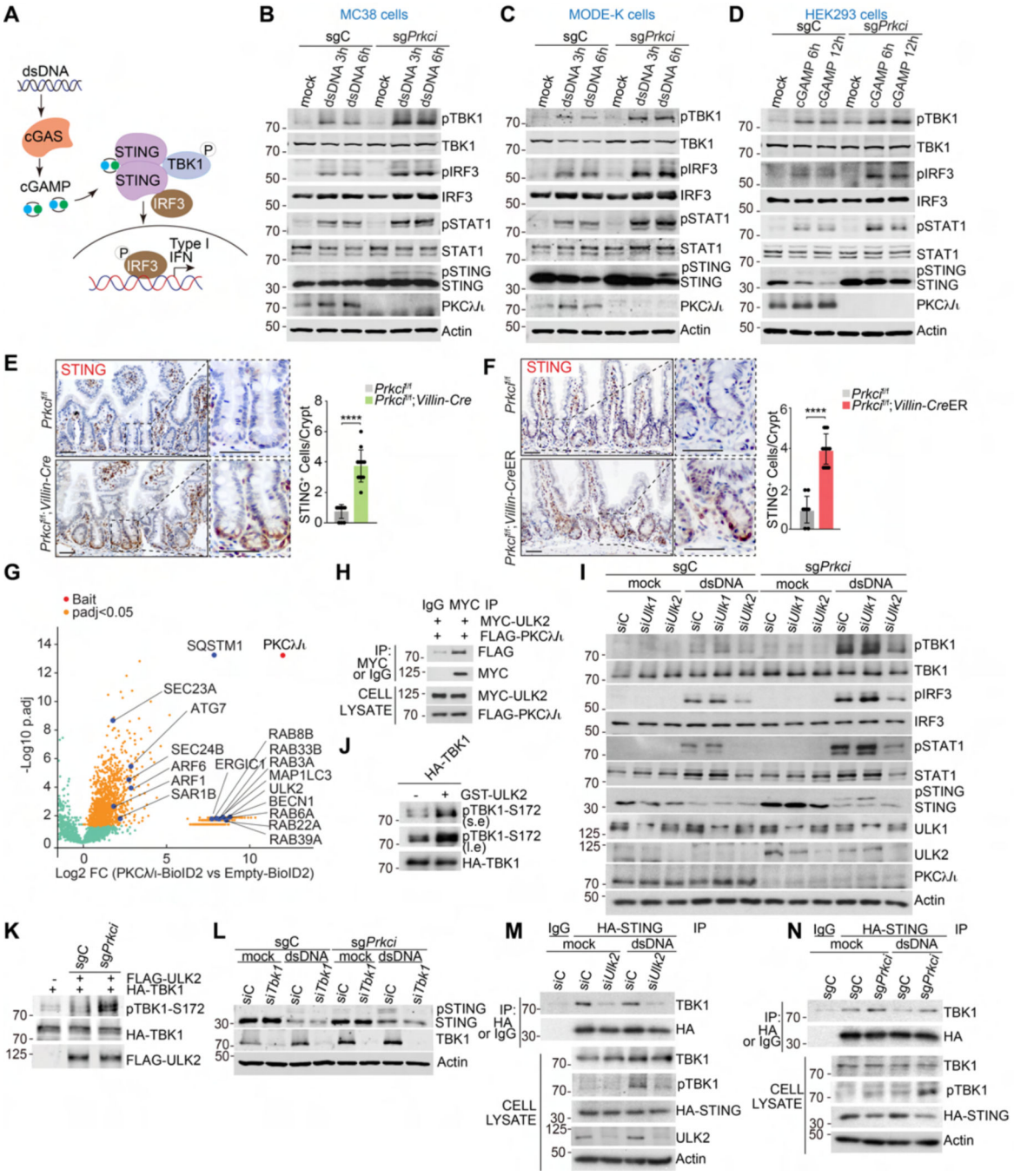

Figure 2. PKCλ/ι interaction with ULK2 is critical for the control of the IFN response through TBK1

(A) Model that represents the role of PKCλ/ι in the repression of the IFN cascade upstream of TBK1 but downstream of cGAS.

(B-D) Immunoblot analysis of indicated proteins in sg*Prkci* and sgC MC38 (B), MODE-K (C) and HEK293 (D) cells transfected with dsDNA, cGAMP or mock transfected for 0, 3 and 6 h (n = 3).

(E) STING staining and quantification of small intestines from *Prkci*$^{f/f}$;*Villin-Cre* and *Prkci*$^{f/f}$ mice. Scale bar, 50 μm.

(F) STING staining and quantification of small intestines from *Prkci*$^{f/f}$;*Villin-Cre*ER and *Prkci*$^{f/f}$ mice. Tamoxifen was injected by oral gavage (240 mg/kg) and mice were sacrificed after 7 days treatment. Scale bar, 50 μm.

(G) Volcano plot of biotinylated proteins in PKCλ/ι-BioID2-dsDNA versus Empty-BioID2 HEK293 cells (n = 3).

(H) Immunoblotting of cell lysate and MYC-tagged immunoprecipitates of HEK293T cells transfected with the indicated plasmid and treated with Bafilomycin A1 (100 nM, 12 h).

(I) Immunoblot analysis of indicated proteins in sg*Prkci* and sgC MODE-K cells transfected with scramble siRNA, (siC), si*Ulk1* or si*Ulk2.* After 48 h, cells were transfected with dsDNA or mock transfected for 6 h (n = 3).

(J) Immunoblot analysis of *in vitro* kinase assay performed with GST-ULK2 active kinase (baculovirus-expressed recombinant protein) and immunoprecipitated HA-tagged TBK1 as substrate (n = 3).

(K) Immunoblot analysis of *in vitro* kinase assay performed with FLAG-tagged ULK2 immunopreciptated from sg*Prkci* or sgC HEK293T cells and immunoprecipitated HA-tagged TBK1 as substrate (n = 3).

(L) Immunoblot analysis of indicated proteins in sg*Prkci* and sgC MODE-K cells transduced with the indicated siRNA. After 48 h, cells were transfected with dsDNA or mock transfected for 6 h.

(M) Immunoblotting of cell lysates and HA-tagged immunoprecipitates of MODE-K cells, expressing HA-tagged STING, transduced with the indicated siRNA and transfected with dsDNA or mock transfected for 6 h.

(N) Immunoblotting of cell lysates and HA-tagged immunoprecipitates of sg*Prkci* and sgC MODE-K cells expressing HA-tagged STING and transfected with dsDNA or mock transfected for 6 h.

Results are shown as mean ± SEM ****$p < 0.0001$. See also Figure S2.

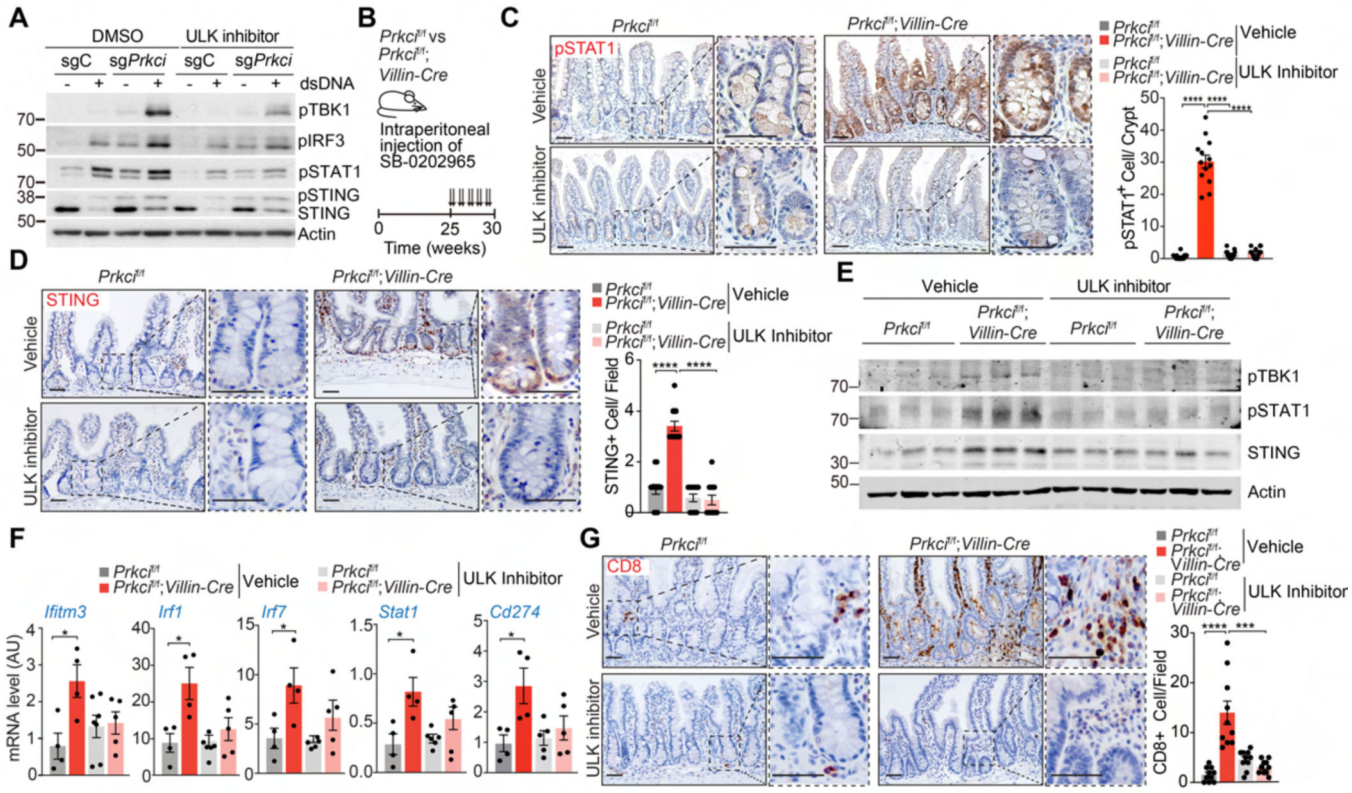

Figure 3. The pharmacological inhibition of ULK1/2 reduces the IFN response promoted by PKCλ/ι-deficiency

(A) Immunoblot analysis of indicated proteins in sg*Prkci* and sgC MODE-K cells treated with SBI-0202965 or vehicle for 6 h and transfected with dsDNA, or mock transfected for 6 h (n = 3).

(B-D) Pharmacological Inhibition of ULK1/2 *in vivo*. Experimental design (B), pSTAT1 (C) or STING (D) staining and quantification of small intestines from *Prkci*$^{f/f}$;*Villin-Cre* and *Prkci*$^{f/f}$ mice treated with SBI-0202965 or vehicle. (n: *Prkci*$^{f/f}$ Vehicle = 5, *Prkci*$^{f/f}$ SBI-0202965 treated = 5, *Prkci*$^{fl/fl}$-*Villin-Cre* Vehicle = 5, and *Prkci*$^{fl/fl}$-*Villin-Cre* SBI-0202965 treated = 5). Scale bar, 50 μm.

(E) Immunoblot analysis of indicated proteins in IECs from *Prkci*$^{f/f}$;*Villin-Cre* and *Prkci*$^{f/f}$ mice treated with SBI-0202965 or vehicle.

(F) qRT-PCR analysis of mRNA levels of IFN-related genes in IECs from *Prkci*$^{f/f}$;*Villin-Cre* and *Prkci*$^{f/f}$ mice treated with SBI-0202965 or vehicle

(G) CD8 staining and quantification of small intestines from *Prkci*$^{f/f}$;*Villin-Cre* and *Prkci*$^{f/f}$ mice treated with SBI-0202965 or vehicle. (n: *Prkci*$^{f/f}$ Vehicle = 5, *Prkci*$^{f/f}$ SBI-0202965 treated = 5, *Prkci*$^{fl/fl}$-*Villin-Cre* Vehicle = 5, and *Prkci*$^{fl/fl}$-*Villin-Cre* SBI-0202965 treated = 5). Scale bar, 50 μm.

Results are shown as mean ± SEM *p < 0.05, ***p < 0.001, ****p < 0.0001.

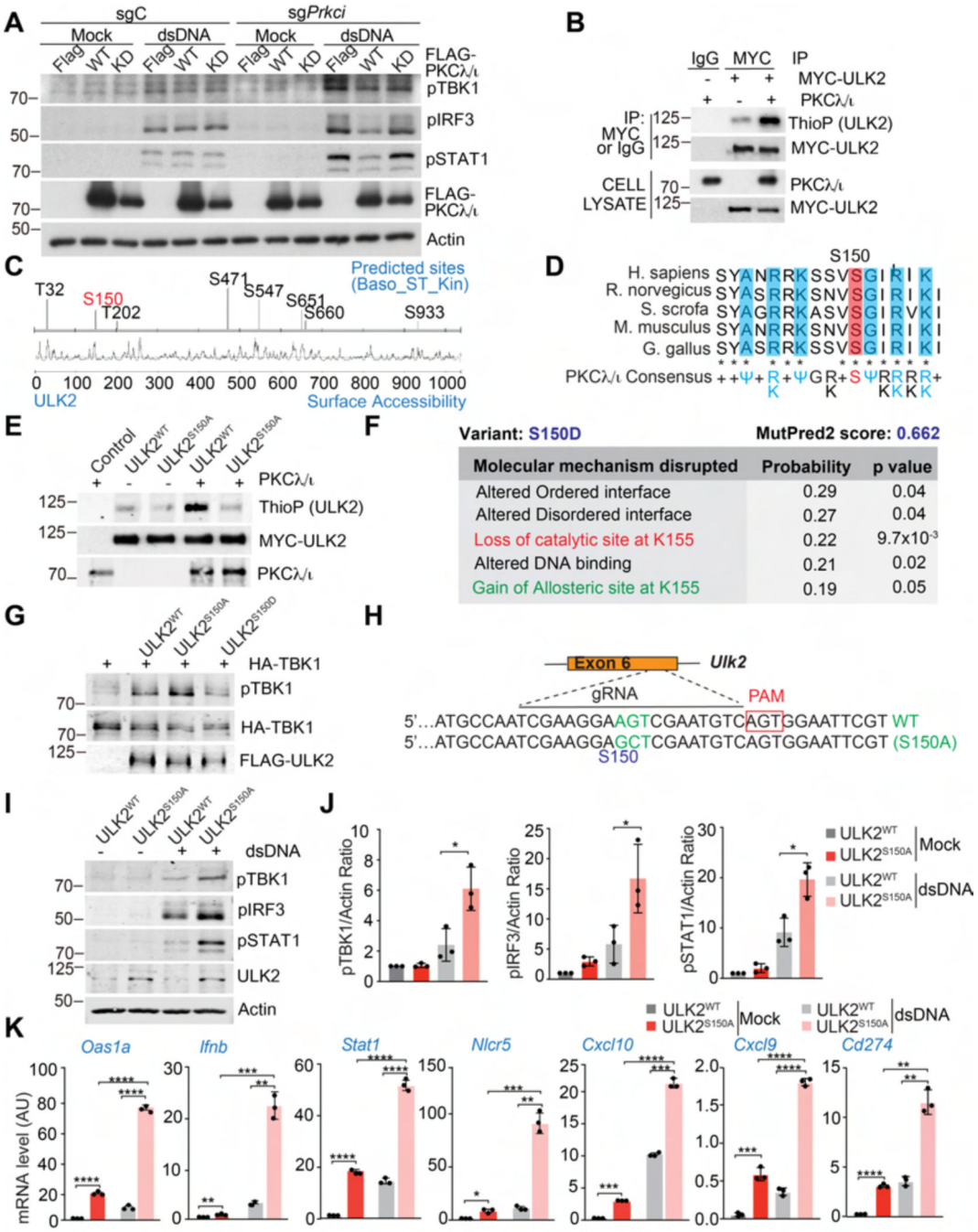

Figure 4. PKCλ/ι directly represses ULK2 kinase activity

(A) Immunoblot analysis of indicated proteins in sg*Prkci* and sgC MODE-K cells expressing either Flag-tagged empty vector, Flag-tagged PKCλ/ι WT or FLAG-tagged PKCλ/ι kinase-dead and transfected with dsDNA or mock transfected for 6 h (n = 3).

(B) *In vitro* phosphorylation of MYC-tagged ULK2 by recombinant PKCλ/ι with ATPγS followed by p-nitrobenzyl mesylate (PNBM) alkylation and immunoblotting for the indicated proteins.

(C) Predicted sites of phosphorylation of PKCλ/ι in human ULK2 by Scansite 4.0 software.

(D) Alignment of the amino acid sequence of human ULK2 (140–155 aa) with orthologs in other species, in comparison with PKCλ/ι consensus sequence.
(E) *In vitro* phosphorylation of MYC-tagged ULK2 WT or ULK2 S150A by a recombinant PKCλ/ι with ATPγS followed by PNBM alkylation and immunoblotting for the indicated proteins.
(F) Predicted functional alterations in ULK2 phosphorylation at S150 by Mutpred2 software.
(G) *In vitro* phosphorylation of HA-tagged TBK1 by Flag-tagged ULK2 WT, ULK2 S150A or ULK2 S150D, and immunoblotting for the indicated proteins.
(H) Schematic representation of endogenous *Ulk2* editing in MODE-K cells.
(I and J) Immunoblot analysis of indicated proteins in WT ($ULK2^{WT}$) and S150A ($ULK2^{S150A}$) MODE-K cells transfected with dsDNA or mock transfected for 6 h (I) and quantification of pTBK1, pIRF3 and pSTAT1 intensity normalized to actin (J) (n = 3).
(K) qRT-PCR analysis of mRNA levels of IFN-related genes in $ULK2^{WT}$ and $ULK2^{S150A}$ MODE-K cells transfected with dsDNA or mock transfected for 6 h (n = 3).
Results are shown as mean ± SEM *p < 0.05 **p < 0.01, ***p < 0.001, ****p < 0.0001.

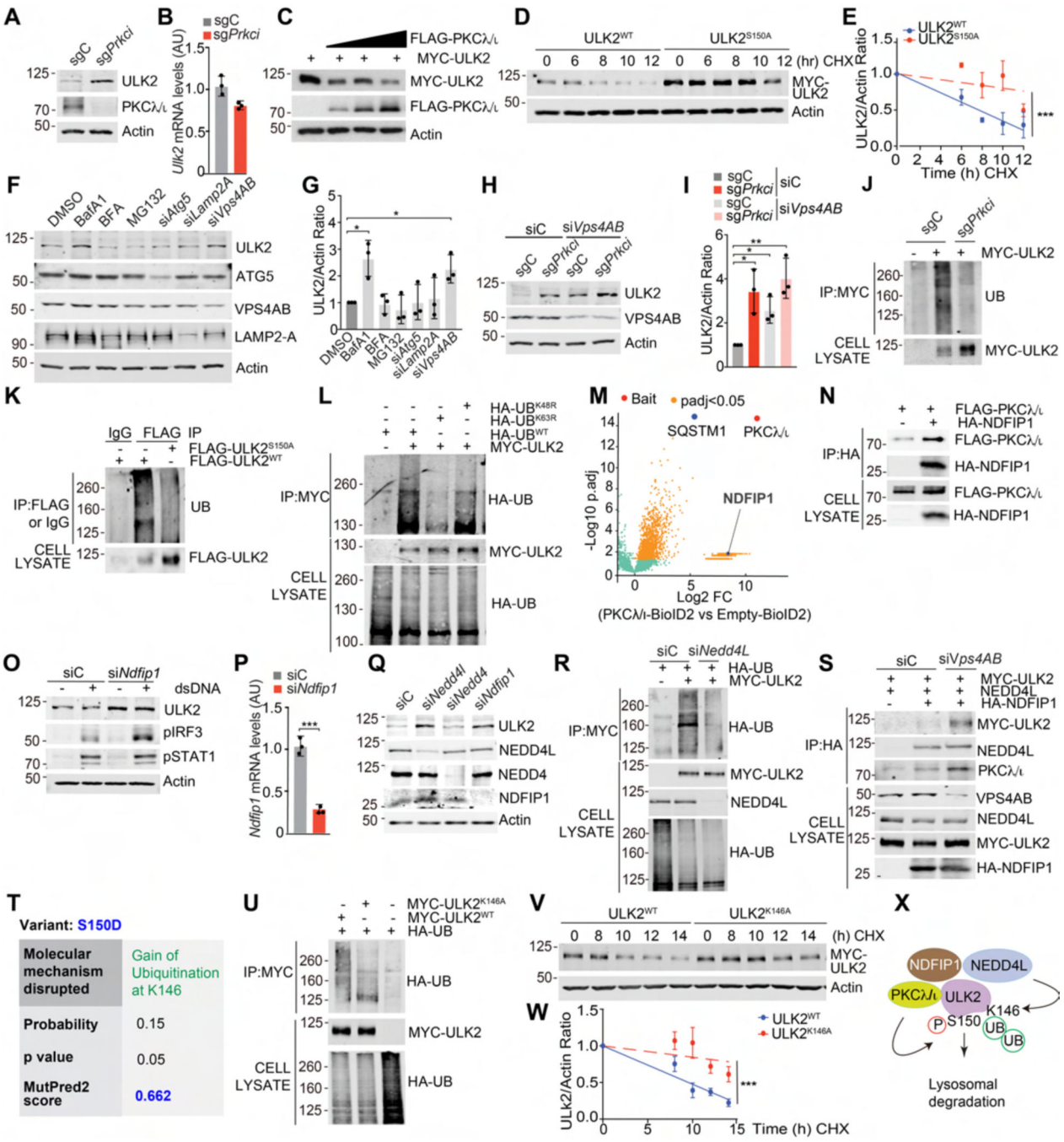

Figure 5. PKCλ/ι regulates ULK2 levels through a ubiquitin-dependent lysosomal degradation mechanism

(A and B) Immunoblot analysis of indicated proteins (A) and qRT-PCR analysis (B) of mRNA of *Ulk2* in sg*Prkci* and sgC MODE-K cells (n = 3).

(C) Immunoblot analysis of HEK293T cells transfected with the indicated plasmids.

(D and E) HEK293T cells, transfected with the indicated plasmids, were incubated with 50 ug/ml of cycloheximide (CHX) and protein stability was determined by immunoblotting at indicated time points (D). ULK2 levels were normalized to actin (E) (n = 3).

(F and G) Immunoblot analysis of indicated proteins in MODE-K cells transduced with the indicated siRNAs or treated with Bafilomycin A1 (100 nM), MG132 (20 μM) or Brefeldin (BFA) (10 μM) for 12 h (F) and quantification of ULK2 intensity normalized to actin (G) (n = 3).

(H and I) Immunoblot analysis of indicated proteins in MODE-K cells transduced with the indicated siRNAs (H) and quantification of ULK2 intensity normalized to actin (I) (n = 3).

(J) Immunoblotting of cell lysate and MYC-tagged immunoprecipitates of sg*Prkci* and sgC MODE-K cells, transfected with the indicated plasmids.

(K and L) Immunoblotting of cell lysate and FLAG-tagged immunoprecipitates (K) or MYC-tagged immunoprecipitates (L) of MODE-K cells, transfected with the indicated plasmids.

(M) Volcano plot showing NDFIP1 among the biotinylated proteins in PKCλ/ι-BioID2-dsDNA versus Empty-BioID2 HEK293 cells (n = 3).

(N) Immunoblotting of cell lysate and HA-tagged immunoprecipitates of HEK293T cells transfected with the indicated plasmids.

(O and P) Immunoblot analysis of indicated proteins in MODE-K cells transduced with the indicated siRNAs and transfected with dsDNA or mock transfected for 6 h (O) and qRT-PCR analysis of mRNA levels of *Ndfip1* (P).

(Q) Immunoblot analysis of indicated proteins in MODE-K cells transduced with the indicated siRNAs.

(R) Immunoblotting of cell lysate and MYC-tagged immunoprecipitates of MODE-K cells, transduced with the indicated siRNAs and the indicated plasmids.

(S) Immunoblotting of cell lysate and HA-tagged immunoprecipitates of HEK293T cells, transduced with the indicated siRNAs and the indicated plasmids.

(T) Predicted functional alterations in ULK2 phosphorylation at S150 by Mutpred2 software.

(U) Immunoblotting of cell lysate and MYC-tagged immunoprecipitates of MODE-K cells transfected with the indicated plasmids.

(V and W) HEK293T cells, transfected with the indicated plasmids, were incubated with 50 ug/ml of cycloheximide (CHX) and protein stability was determined by immunoblotting at indicated time points (V). ULK2 levels were normalized to actin (W) (n = 3).

(X) Model that represents that ULK2 phosphorylation by PKCλ/ι at S150 serves to promote its K63 ubiquitination in an NDFIP1-NEDD4L dependent manner.

Results are shown as mean ± SEM *p < 0.05, **p < 0.01, ***p < 0.001. See also Figure S3.

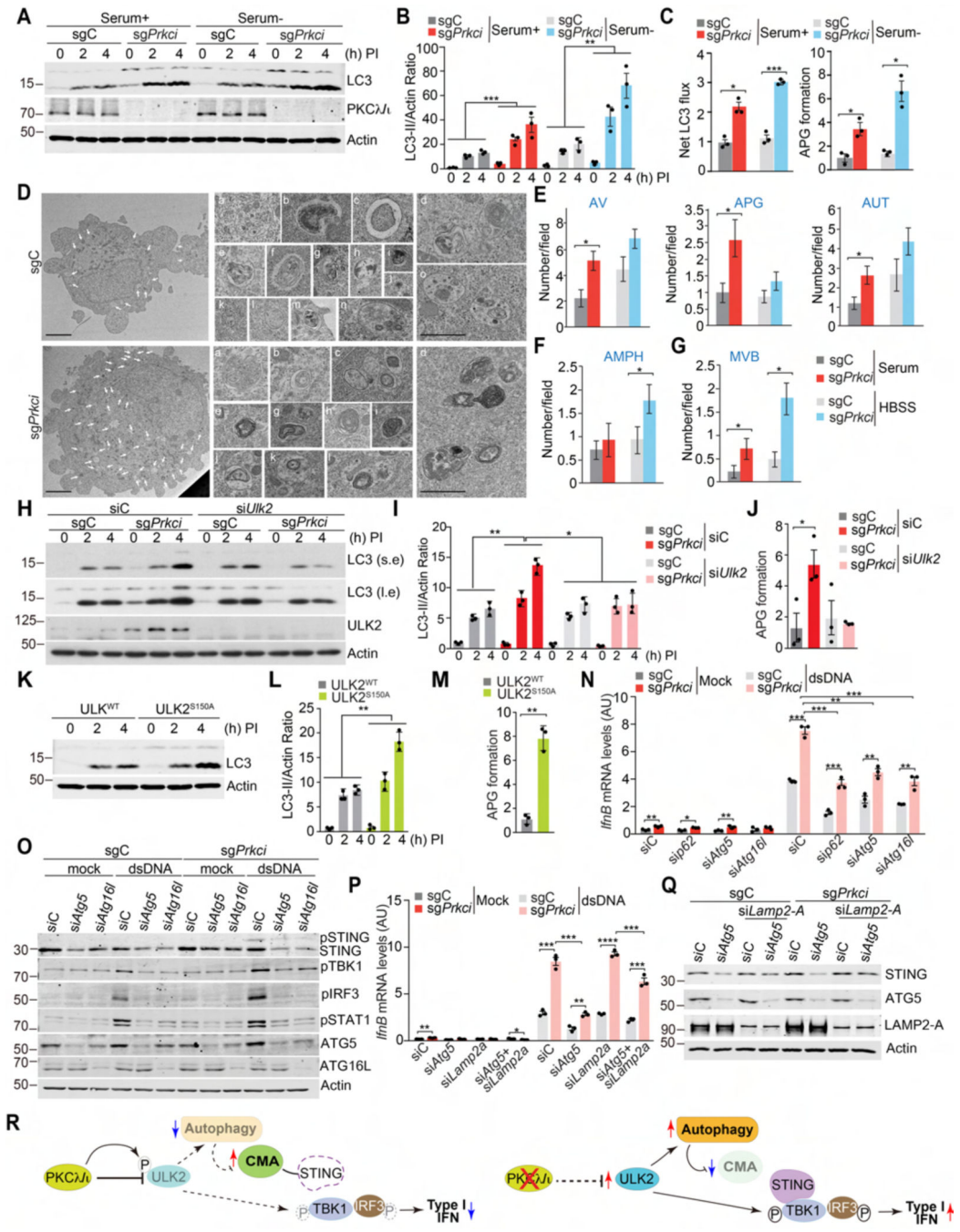

Figure 6. PKCλ/ι represses autophagy through an ULK2-dependent mechanism

(A and B) Immunoblot for LC3 in response to lysosomal inhibitors (PI) (A) and quantification of LC3-II intensity normalized to actin (B) in sg*Prkci* and sgC MODE-K cells in presence or absence of serum (n = 3).

(C) Calculated net LC3 flux and speed of autophagosome formation from cells treated as in (A) (n = 3).

(D) Electron microscopy (EM) images of sg*Prkci* and sgC MODE-K cells in serum-supplemented media (Serum) or Hank's balanced salt solution (HBSS). Arrows

indicate autophagy-related compartments. Insets show at higher magnification examples of autophagic vacuoles and amphisomes in different stages of maturation. In sgC cells: a (autophagosome), b-f (inmature autolysosomes), g-j (autolysosomes), k,l (multivesicular body), m-o (amphisomes). In sg*Prkci* cells: a (autophagosome), b,c (inmature autolysosomes), d-i (autolyssoomes), j-l (amphisomes). Scale bar, 1 μm.

(E-G) Quantification of the average number of autophagosomes (APG), autolysosomes (AUT), autophagic vacuoles (AV), amphisomes (AMPH), multivesicular bodies (MVB). At least 14 different fields were quantified.

(H and I) Immunoblot for LC3 in response to lysosomal inhibitors (PI) (H) and quantification of LC3-II intensity normalized to actin (I) in sg*Prkci* and sgC MODE-K cells, transduced with the indicated siRNAs (n = 3).

(J) Calculated speed of autophagosome formation from cells treated as in (H) (n = 3).

(K and L) Immunoblot for LC3 in response to lysosomal inhibitors (K) and quantification of LC3-II intensity normalized to actin (L) in WT and S150A MODE-K cells (n = 3), (M) Calculated speed of autophagosome formation from cells treated as in (K) (n = 3).

(N) qRT-PCR analysis of mRNA levels of *IfnB* in sg*Prkci* and sgC MODE-K cells, transduced with the indicated siRNAs and transfected with dsDNA or mock transfected for 6 h (n = 3).

(O) Immunoblot analysis of indicated proteins in sg*Prkci* and sgC MODE-K cells transduced with the indicated siRNAs and transfected with dsDNA or mock transfected for 6 h (n = 3).

(P) qRT-PCR analysis of mRNA levels of *IfnB* in sg*Prkci* and sgC MODE-K cells, transduced with the indicated siRNAs and transfected with dsDNA or mock transfected for 6 h (n = 3).

(Q) Immunoblot analysis of indicated proteins in sg*Prkci* and sgC MODE-K cells transduced with the indicated siRNAs.

(R) Scheme shows that increased autophagy in PKCλ/ι-deficient cells prevents the inactivation of the IFN pathway by CMA-driven degradation of STING.

Results are shown as mean ± SEM *p < 0.05, **p < 0.01, ***p < 0.001. ****p < 0.0001. See also Figure S4.

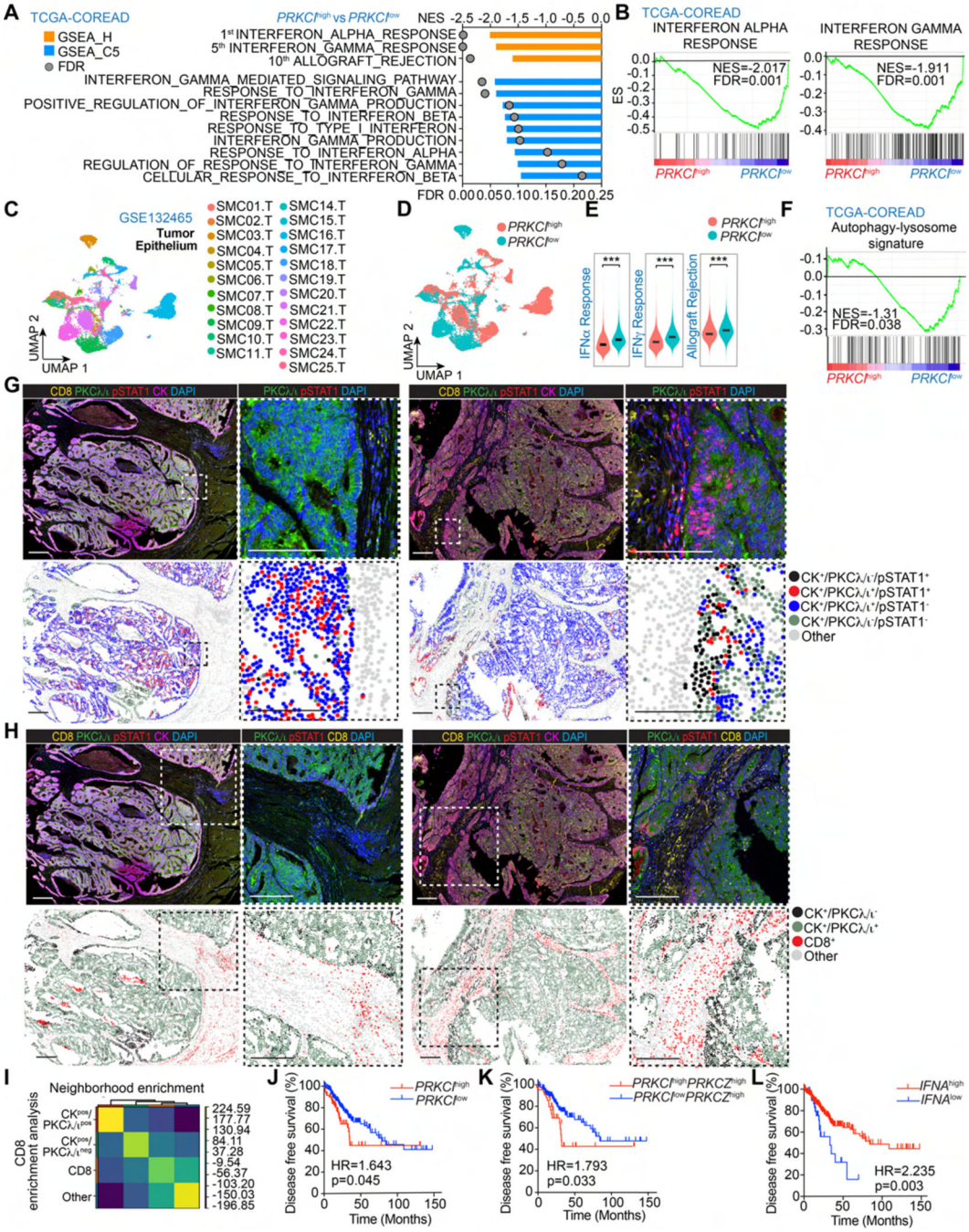

Figure 7. PKCλ/ι-deficiency in the intestinal epithelium drives IFN activation in vivo and anti-cancer immunosurveillance

(A) GSEA of transcriptomic data of colorectal cancer (CRC) samples (TCGA) stratified on the basis of *PRKCI* expression. Indicated gene signatures from the Hallmark and C5 collection of MSigDB were applied to the analyses. Normalized enrichment scores (NES) and False discovery rate (FDR) are shown.

(B) GSEA plots of enrichment in the indicated gene signatures from MsigDB in CRC patient samples from TCGA stratified by *PRKCI* expression.

(C) Uniform Manifold Approximation and Projection (UMAP) plot with clustering results colored by samples of tumor epithelium from CRC patients (GSE132465).
(D) UMAP plot of the tumor epithelium compartment of CRC patients (GSE132465) stratified on the basis of *PRKCI* expression.
(E) Violin plots for the indicated gene signatures in CRC patients (GSE132465) stratified on the basis of *PRKCI* expression.
(F) GSEA plot of enrichment in the indicated gene signature in CRC patient samples from TCGA stratified by *PRKCI* expression.
(G) Five-color overlay image of a selected tissue core and higher magnification three-color images (upper panels). Spatial analysis showing PKCλ/ι/pSTAT1 state among tumor epithelial cells labeled as CK positive (bottom panels).
(H) Five-color overlay image of a selected tissue core and higher magnification three-color images (upper panels). Spatial analysis showing PKCλ/ι state in tumor epithelial cells, and enrichment of CD8 cells (bottom panels).
(I) Representative neighborhood enrichment analysis of CD8 cells in PKCλ/ι negative or positive tumor epithelial cells.
(J) Kaplan-Meier curve for recurrence-free survival of TCGA CRC patients according to *PRKCI* expression.
(K) Kaplan-Meier curve for recurrence-free survival of TCGA CRC patients according to *PRKCI/PRKCZ* expression.
(L) Kaplan-Meier curve for recurrence-free survival of TCGA CRC patients according to *IFNA* score.
Results are shown as mean ± SEM. ***$p < 0.001$. See also Figure S5.

KEY RESOURCES TABLE

REAGENT or RESOURCE	SOURCE	IDENTIFIER
Antibodies		
Mouse anti-β-actin	Sigma-Aldrich	Cat# A1978, RRID: AB_476692
Rabbit anti-SQSTM1/p62	Cell Signaling Technology	Cat# 23214, RRID: AB_11157045
Rabbit anti-STING	Cell Signaling Technology	Cat# 13647, RRID: AB_2732796
Rabbit anti-phospho-TBK1	Cell Signaling Technology	Cat# 5483, RRID: AB_10693472
Mouse anti-TBK1	Santa Cruz Biotechnology	Cat# sc-52957, RRID: AB_783995
Rabbit anti-phospho-IRF3	Cell Signaling Technology	Cat# 4947, RRID: AB_823547
Mouse anti-IRF3	Santa Cruz Biotechnology	Cat# sc-376455, RRID: AB_11151578
Rabbit anti-phospho-STAT1	Cell Signaling Technology	Cat# 9167, RRID: AB_561284
Rabbit anti-STAT1	Santa Cruz Biotechnology	Cat# sc-346, RRID: AB_632435
Rabbit anti-LC3A/B	Cell Signaling Technology	Cat# 4108, RRID: AB_2137703
Rabbit anti-LAMP2A	Abcam	Cat# ab18528, RRID: AB_775981
Rabbit anti-Thiophosphate ester	Abcam	Cat# ab92570, RRID: AB_10562142
Mouse anti-FLAG	Sigma-Aldrich	Cat# F3165, RRID: AB_259529
Mouse anti-PKCλ	BD Biosciences	Cat# 610208, RRID: AB_397607
Rabbit anti-HA-Tag	Cell Signaling Technology	Cat# 3724, RRID: AB_1549585
Mouse anti-GST-tag	Santa Cruz Biotechnology	Cat# sc-138, RRID: AB_627677
Rabbit anti-NEDD4L	Cell Signaling Technology	Cat# 4013, RRID: AB_1904063
Mouse anti-NEDD4	Cell Signaling Technology	Cat# 2740, RRID: AB_2149312
Rabbit anti-NDFIP1	Proteintech	Cat# 15602-1-AP, RRID: AB_2878157
Rabbit anti-ATG5	Cell Signaling Technology	Cat# 12994S, RRID: AB_2630393
Rabbit anti-ULK2	GeneTex	Cat# GTX111476, RRID: AB_1952511
Mouse anti-MYC-Tag	Cell Signaling Technology	Cat# 2040, RRID: AB_2148465
Rabbit anti-ATG16L1	Cell Signaling Technology	Cat# 8089, RRID: AB_10950320
Rabbit anti-ULK1	Cell Signaling Technology	Cat# 8054, RRID: AB_11178668
Mouse anti-UB	Santa Cruz Biotechnology	Cat# sc-8017, RRID: AB_2762364
Mouse anti-VPS4	Santa Cruz Biotechnology	Cat# sc-133122, RRID: AB_2304400
Rat anti-CD8	BD Pharmingen	Cat# 557654, RRID: AB_396769
Mouse anti-CD8	Thermo Fisher Scientific	Cat# MA5-13473, RRID: AB_11000353
Mouse anti-CYTOKERATIN	EMD Millipore	Cat# MAB3412, RRID: AB_94853
Goat anti-Mouse IgG1, secondary, HRP	Thermo Fisher Scientific	Cat# PA1-74421, RRID: AB_10988195
Goat anti-Rabbit IgG, secondary, HRP	Thermo Fisher Scientific	Cat# 31461, RRID: AB_228347
Goat anti-Mouse IgG1, secondary, Alexa Fluor 488	Thermo Fisher Scientific	Cat# A21121, RRID: AB_2535764
Donkey anti-Rat IgG, secondary, Alexa Fluor 488	Thermo Fisher Scientific	Cat# A21208, RRID: AB_2535794
Donkey anti-Rabbit IgG, secondary, Alexa Fluor 568	Thermo Fisher Scientific	Cat# A10042, RRID: AB_2534017
Rat anti-CD16/CD32	BD Pharmingen	Cat# 553142, RRID:AB_394657
Mouse anti-NK1.1	BD Pharmingen	Cat# 553165, RRID:AB_394677

REAGENT or RESOURCE	SOURCE	IDENTIFIER
Rat anti-CD4	BD Horizon	Cat# 560468, RRID:AB_1645271
Rat anti-CD8	BD Pharmingen	Cat# 557654, RRID:AB_396769
Rat anti-CD45	BD Horizon	Cat# 563891, RRID:AB_2734134
Hamster anti-TCRβ chain	BD Pharmingen	Cat# 553174, RRID:AB_398534
Bacterial and virus strains		
DH5α Competent Cells	Thermo Scientific	Cat# 18265017
One Shot Stbl3 Chemically Competent	Thermo Scientific	Cat# C737303
Biological samples		
Human Colorectal cancers (CRC)	Osaka City University Hospital, Osaka, JAPAN	N/A
Chemicals, peptides, and recombinant proteins		
X-tremeGENE transfection reagent	Roche	Cat# 6366236001
Ampicillin	Fisher BioReagents	Cat# BP1760-25
MG132	Sigma-Aldrich	Cat# 474790
Bafilomycin A1	Selleck Chemicals LLC	Cat# S1413
Cyclohexamide	Sigma-Aldrich	Cat# C7698
Chloroquine	Sigma-Aldrich	Cat# C6628
2′3′-cGAMP	InvivoGen	Cat# tlrl-nacga23
Dimethyl Sulfoxide	Fisher BioReagents	Cat# BP2311
ECL Western Blotting Substrate	Thermo Scientific	Cat# 32106
HBSS (no calcium, no magnesium)	Gibco	Cat# 14175095
HEPES	Gibco	Cat# 15630080
L-Glutamine	Corning	Cat# 25-005-CI
Lipofectamine 2000 Transfection Reagent	Invitrogen	Cat# 11668019
Lipofectamine RNAiMAX Transfection Reagent	Invitrogen	Cat# 13778030
Opti-MEM Reduced Serum Medium	Gibco	Cat# 31985070
PBS (no calcium, no magnesium)	Gibco	Cat# 10010-023
Puromycin	Omega Scientific, inc.	Cat# PR-01
QuickChange II Site-Directed Mutagenesis Kit	Agilent	Cat# 200523
Quick-RNA Miniprep Kit	Zymo Research	Cat# R1054
RNA*later* Stabilization Solution	Invitrogen	Cat# AM7021
TRIzol	Thermo Fisher Scientific	Cat# 15596018
DMEM	Corning	Cat# 10-017CV
Advanced DMEM/F12	Thermo Fisher Scientific	Cat# 12634010
GlutaMAX Supplement	Thermo Fisher Scientific	Cat# 35050061
Y-27632	Tocris	Cat# 1254
B27 Supplement	Thermo Fisher Scientific	Cat# 17504001
N2 Supplement	Thermo Fisher Scientific	Cat# 17502048
Murine EGF	Thermo Fisher Scientific	Cat# PMG8045
Recombinant murine R-Spondin	R&D systems	Cat# 3474-RS-050

REAGENT or RESOURCE	SOURCE	IDENTIFIER
Recombinant murine Noggin	Peprotech	Cat# 250-38
Collagenase type XI	Sigma-Aldrich	Cat# C7657
Matrigel® Growth Factor Reduced (GFR) Basement Membrane Matrix	Corning	Cat# 356230
Recombinant human PKCi kinase	Thermo Fisher Scientific	Cat# PV3186
Recombinant human ULK2 kinase	Sigma-Aldrich	Cat# SRP5097
Polybrene Infection Reagent	Sigma-Aldrich	Cat# TR-1003-G
TrueCut Cas9 Protein v2	Thermo Fisher Scientific	Cat# A36498
Tamoxifen	Sigma-Aldrich	Cat# T5648
4-OH-tamoxifen	Millipore-Sigma	Cat# H7904
Azoxymethane	Sigma-Aldrich	Cat# A5486
Dextran Sulfate Sodium Salt (DSS) - Colitis Grade (36,000 – 50,000 MW)	MP biomedicals	CAS Number: 9011-18-1
SBI-0206965	SelleckChem	Cat# S7885
Percoll	GE Healthcare	Cat# GE17-0891-01
Critical commercial assays		
Fixation/Permeabilization solution kit	BD Cytofix/Cytoperm™	Cat# 554714
VECTASTAIN® Elite® ABC-HRP Kit	Vector	Cat# PK-6100
Neon™ 10µl Electroporation Kit	Thermo Fisher Scientific	Cat# MPK1096
Automated Opal 7-Color IHC Kit	AKOYA BIOSCIENCES	Cat# NEL821001KT
Deposited data		
RNA-seq (*Prkci*$^{f/f}$ and *Prkci*$^{f/f}$; *Villin*-Cre IECs)	(Nakanishi et al., 2018)	GEO:GSE109289
ATAC-seq (*Prkci*$^{f/f}$ and *Prkci*$^{f/f}$; *Villin*-Cre IECs)	This study	GEO:GSE180223
3’ RNA-seq (*sgPrkci* and sgC MTOs)	This study	GEO:GSE180222
Proteomics (Flag and Flag-PKCλ 293T cells)	This study; Mendeley Data	doi: 10.17632/tpjcr237pz.1
Raw Data	This study; Mendeley Data	doi: 10.17632/tpjcr237pz.1
Microarray from Crohn’s disease and Ulcerative Colitis colonic specimens	(Montero-Melendez et al., 2013)	GEO:GSE36807
Microarray from endoscopic-derived intestinal mucosal biopsies from patients with Inflammatory Bowel Disease (IBD) and controls	(Vanhove et al., 2015)	GEO:GSE59071
Microarray from patients with Crohn’s disease and Ulcerative Colitis	(Kugathasan et al., 2008)	GEO:GSE10616
Microarray from (un)inflamed colon of patients with Ulcerative Colitis	(Van der Goten et al., 2014)	GEO:GSE48958
Microarray from patients with Ulcerative Colitis	(Olsen et al., 2009)	GEO:GSE9452
Microarray from patients with inflammatory bowel disease	(Arijs et al., 2009)	GEO:GSE16879
Microarray from patients with moderate-to-severe active Ulcerative Colitis	(Toedter et al., 2011)	GEO:GSE23597
Single cell 3’ RNA sequencing from patients with CRC	(Lee et al., 2020)	GEO:GSE132465
TCGA-COREAD	cBioportal	http://www.cbioportal.org/index.do
Experimental models: Cell lines		

REAGENT or RESOURCE	SOURCE	IDENTIFIER
Mouse MODE-K	Gift from Richard S. Blumberg, Ph.D.	N/A
Mouse MODE-K (S150A)	This study	N/A
Mouse MC38	Kerafast	Cat# ENH204, RRID: CVCL_B288
Human HEK293T	ATCC	Cat# CRL-3216, RRID: CVCL_0063
Human Phoenix-GP	ATCC	Cat# CRL-3215, RRID: CVCL_H718
Mouse tumor organoid (MTO)	(Tauriello et al., 2018)	N/A
Experimental models: Organisms/strains		
Mouse: *Prkci*$^{f/f}$	(Nakanishi et al., 2016)	N/A
Mouse: B6.Cg-Tg(Vil1-cre)997Gum/J (*Villin-cre*)	The Jackson Laboratories	Stock No: 004586
Mouse: B6.Cg-Tg(Vil1-cre/ERT2)23Syr/J	The Jackson Laboratories	Stock No: 020282
Oligonucleotides		
Real-time PCR primers		Table S1
siRNA oligonucleotides and guides		Table S2
Recombinant DNA		
pBABE-puro-myc-BioID2	Addgene	Cat# 80900
pBABE-puro-myc-BioID2-PKCi	(Kudo et al., 2020)	N/A
pcDNA3	Invitrogen	Cat# V79020
pBABE-puro-mCherry-eGFP-LC3B	Addgene	Cat# 22418
Lentiviral packaging plasmid psPAX2	Addgene	Cat# 12260
Lentiviral packaging plasmid pMD2.G	Addgene	Cat# 12259
pSuper-shRNA targeting mouse *Lamp2a*	(Massey et al., 2006)	N/A
LentiCRISPR v2	Addgene	Cat# 52961
pCMV-FLAG-p62	(Duran et al., 2011)	N/A
pCMV-FLAG-PKCi	(Reina-Campos et al., 2019)	N/A
pCMV-FLAG-PKCi (K274W)	(Reina-Campos et al., 2019)	N/A
pRK5-myc-ULK2	Addgene	Cat# 31966
pRK5-myc-ULK2 (S150A)	This study	N/A
pRK5-myc-ULK2 (S150D)	This study	N/A
pRK5-myc-ULK2 (K146A)	This study	N/A
pDONR223-NDFIP1	DNAsu	HsCD00353216
pENTR223-TBK1	DNAsu	HsCD00505584
pDONR221-ULK2	DNAsu	HsCD0086056
pDONR223-TMEM173	DNAsu	HsCD00353006
pCSF107mT-Gateway-Flag	Addgene	Cat# 67619
pCSF107mT-Gateway-HA	Addgene	Cat# 67616
pCSF107mT-Flag-ULK2	This study	N/A
pCSF107mT-Flag-ULK2 S150A	This study	N/A
pCSF107mT-Flag-ULK2 S150D	This study	N/A
pCSF107mT- HA-STING	This study	N/A

REAGENT or RESOURCE	SOURCE	IDENTIFIER
pCSF107mT- HA-TBK1	This study	N/A
pCSF107mT- HA-NDFIP1	This study	N/A
pDNA3 HA-UB	Addgene	Cat# 18712
pDNA3 HA-UB K48R	(Linares et al., 2013)	N/A
pDNA3 HA-UB K63R	(Linares et al., 2013)	N/A
Software and algorithms		
Graphpad Prism 8	Graphpad	https://www.graphpad.com/scientificsoftware/
ImageJ	NIH	https://imagej.nih.gov/ij/
RStudio (1.1.456)	R Core Team	https://www.r-project.org/
R	R Core Team	https://www.r-project.org/
GSEA (v4.1.0)	Broad Institute	http://www.broadinstitute.org/gsea/index.jsp
BaseSpace	Illumina	https://basespace.illumina.com/
Morpheus	Broad Institute	https://software.broadinstitute.org/morpheus/
Scansite v4.0	Koch Institute	https://scansite4.mit.edu/4.0/#home
NextBio	Illumina	https://nextbio.com
GenePattern	Broad Institute	https://cloud.genepattern.org/gp/pages/login.jsf
Mutpred2	(Pejaver et al., 2020)	http://mutpred.mutdb.org/
iUbiq-Lys	(Qiu et al., 2015)	http://www.jci-bioinfo.cn/iUbiq-Lys
Phosphosite	Cell Signaling Technology	http://www.phosphosite.org
Lexogen QuantSeq DE 1.3.0	BlueBee Cloud	https://www.bluebee.com
Bowtie2-2.3.4.3	(Langmead and Salzberg, 2012)	N/A
Taiji 1.1.0	(Zhang et al., 2019)	N/A
Seurat 3.0	(Stuart et al., 2019)	https://github.com/Satijalab/seurat
Scanpy Python package	(Wolf et al., 2018)	https://github.com/theislab/Scanpy
GSVA	(Hanzelmann et al., 2013)	https://github.com/rcastelo/GSVA
Survminer R package	N/A	https://github.com/Kassambara/survminer
FlowJo	Tree Star Inc.	N/A
Other		
EVOS FL Auto Imaging System	Thermo Fisher Scientific	N/A
EVOS XL Core Cell Imaging System	Thermo Fisher Scientific	N/A
NanoDrop 1000 spectrophotometer	Thermo Fisher Scientific	N/A
TissueLyser II	QIAGEN	Cat# 85300
Zeiss LSM 710 NLO Confocal Microscope	Carl Zeiss Microscopy	N/A
Nikon A1R HD Confocal Microscope	Nikon	N/A
Philips CM-100 Transmission Electron Microscope	Philips Electron Optics	N/A
Neon™ Transfection System	Thermo Fisher Scientific	Cat# MPK5000
BOND RX Automated IHC stainer	Leica	N/A

REAGENT or RESOURCE	SOURCE	IDENTIFIER
Vectra Polaris Automated Quantitative Pathology Multispectral Imaging System	AKOYA BIOSCIENCES	N/A
FACSymphony™ A5 Cell Analyzer	BD Biosciences	N/A